LAWRENCE
LIVERMORE
NATIONAL
LABORATORY

LLNL-JRNL-868814

Diamond Under Extremes

A. C. Li, B. Li, F. Gonzalez-Cataldo, R. E. Rudd, B. Militzer, E. M. Bringa, M. A. Meyers

August 28, 2024

Materials Science and Engineering: Reports

Disclaimer

Diamond Under Extremes

Alex C. Li,[1, a)] Boya Li,[1] Felipe González-Cataldo,[2] Robert E. Rudd,[3] Burkhard Militzer,[2, 4] Eduardo M. Bringa,[5] and Marc A. Meyers[1, a)]

[1]*Program of Materials Science and Engineering, University of California, San Diego, USA*

[2]*Department of Earth and Planetary Science, University of California, Berkeley, California, USA*

[3]*Materials Science Division, Lawrence Livermore National Laboratory, Livermore, USA*

[4]*Department of Astronomy, University of California, Berkeley, California, USA*

[5]*CONICET and Facultad de Ingeniería, Universidad de Mendoza, Mendoza, Argentina*

[a)]Co-corresponding authors: acl005@ucsd.edu, mameyers@ucsd.edu

Diamond is, by virtue of the covalent bonding between atoms and the very strong carbon to carbon bonds, the hardest natural material. It has been a fascinating material since its discovery, first as a decorative gem and more recently, for its numerous industrial uses because of its extreme hardness, elastic modulus, and optical transparency. In recent years, it has become a preferred ablator for laser shock experiments, and this has led to its choice as the capsule material for fusion experiments at the National Ignition Facility. This review covers both experimental and computational advancements in research on diamond subjected extreme conditions of temperature and pressure. The synergy between shock and ramp loading experiments and atomic level simulations is proving to be powerful in advancing our understanding of diamond under extremes.

Contents

1. Introduction

Carbon is sometimes called the "king of the elements" [1] because of its amazing ability to bond with both itself and other elements. After H, He, and O, carbon is the most common element in the universe, and is intimately connected with life on earth. Whether as a part of organic material bonded to many other elements such as oxygen and hydrogen or in its elemental form as graphite or diamond, carbon is a part of so much of the world around us. Even in just its elemental forms, its applications are diverse and dependent upon its morphology, whether from the nanoscale properties of carbon nanotubes and graphene, or to the bulk properties of solid diamond. Its resilience, luster, and clarity have made it popular for jewelry that symbolizes of unending devotion, while its more practical applications in industry include use in diamond saws or polishing agents, where its high hardness and strength allows it to act as an abrasive for removing other, softer material.

Under the immense pressures found in planetary interiors, carbon adopts the diamond phase, which is the only stable allotrope that exists up to pressure of 1 terapascal. At higher pressure (>1 TPa) calculations predict a body-centered cubic structure (BC8) and at even higher pressure (>3 TPa) a simple cubic structure is predicted to be stable. A fourth structure, simple hexagonal, has also been observed after shock synthesis and in the Carbonado diamond that is the result of meteoric impact. Figure 1 shows the atomic arrangements of the four structures. Understanding these phase transitions holds the key to unlocking technological applications. Carbon may also be important to our understanding of the composition of some distant planets. Closer to the Earth, analysis from the Messenger Orbiter may be compatible with the claim that there is a 17 km diamond layer at the interface between the mantle and core of Mercury [2].

While theories predict a new carbon phase—BC8 (body-centered with each atom heaving eight nearest neighbors)—emerging at pressures beyond 1 TPa, experimental evidence remains elusive. The mechanisms by which diamond transitions to this new phase are just being investigated by advanced computational simulations [3], but probing these conditions is very challenging for experiments. Traditional

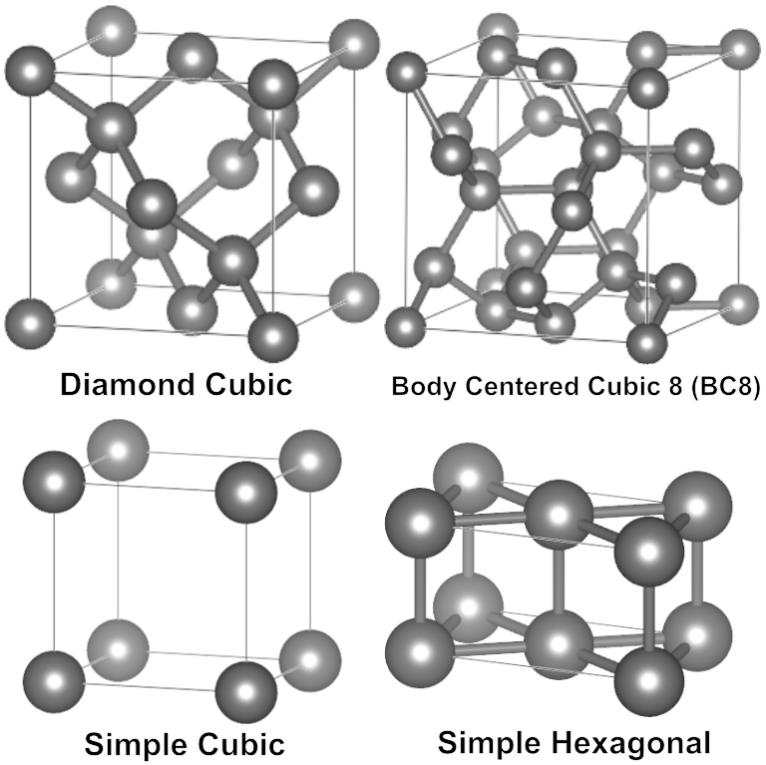

FIG. 1. Unit cells for different stable and metastable phases of Diamond.

methods like shock compression face limitations, often reaching the melting point before achieving the desired pressure.

However, recent efforts through the ramp compression technique [4] have allowed shockless loading that enables access to TPa pressures with decreased temperature rise, maintaining the sample in the solid phase [5]. Remarkably, recent experiments compressed diamond to a staggering 5 terapascals using this method [6], yet no signs of a phase transition to BC8 were observed [7].

The combination of cutting-edge ramp compression with sophisticated characterization tools to bridge the gap between theory and reality should not only confirm the existence of BC8 but also unlock its synthesis pathway, paving the way for carbon's implications upon planetary understanding and materials science advancements.

In this review article, we focus on the properties and uses of carbon diamond under extremes, where

some of its unique properties make it an attractive choice for experiments working at the highest temperatures and pressures one can achieve. In comparison to other Group IV elements on the periodic table which exhibit similar bonding behavior, diamond has a strength of 95 GPa, almost 5 times that of both silicon and germanium, and a shear strength of almost 15 times [8, 9]. This order of magnitude difference comes from the strength of the sp3 covalent bonds between the carbon atoms. This extreme strength makes it attractive for applications that require high pressures, such as its use as the confining material in diamond anvil cells. A combination of this material strength and other factors such as its thermal conductivity, density, optical transparency and other factors have also made diamond the material of choice as an ablator for high energy density experiments, such as forming the capsules which hold the fuel in current National Ignition Facility experiments for controlled fusion research [10].

2. Diamond Synthesis

Natural diamonds form deep beneath the earth's surface, involving the reduction of carbonates and oxidation of methane to form diamond crystals within kimberlite [11]. This kimberlite is carried up closer to the earth's surface by the exsolution of carbon dioxide from the mineral-rich magma [12].

It was not until the 1950s that diamond was reproducibly synthesized by researchers at General Electric, dissolving graphite in molten transition metals under high pressures and high temperatures. Calculations of carbon's phase diagram gave scientists an idea of the temperatures and pressures that were needed for the conversion from the more common graphite phase into the metastable diamond phase. Improvements to pressure vessels finally enabled the achievement of up to 10 GPa pressure and over 2300 K temperature, leading to the first synthesized diamonds [13, 14].

Further research into the synthesis of diamonds yielded several other methods to produce them by imposing thermodynamically favorable conditions to convert graphite to diamond, whether through flash-heating at high static pressure [15] or synthesis through shock [16]. However, the now dominant method of synthesizing diamond came about with advancements in chemical vapor deposition (CVD) processes using gaseous hydrocarbons in an excess of hydrogen [17–19]. This method involves the preferential

nucleation and growth of diamond crystals at pressures and temperatures where graphite should be the more stable form. Subsequent research developed enhancements involving the methods for controlling the activation of the gas-phase carbon precursors, such as use of plasma jets or combustion flame synthesis [20–23]. While growth rates for these diamond films were measured in hours per micrometer in the early stages of the technology, modern growth rates in CVD diamond synthesis can be measured in hundreds of micrometers per hour [24, 25]. The enhanced growth speed and controllability of these CVD processes are what allow the precise design and implementation of diamond for use in research today. As the technology matures it has become possible to produce single crystalline diamond wafers of increasing size and perfection, as seen in Figure 2 [26].

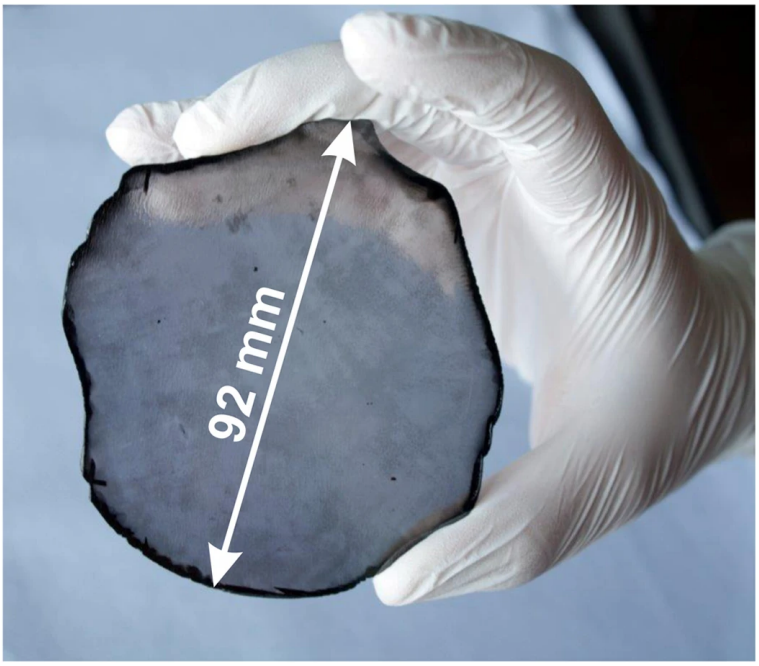

FIG. 2. A large 155 carat (31 grams) single crystal diamond wafer, heteroepitaxially grown via ion bombardment on a Ir/YSZ/Si 001 substrate. (taken from Ref. [26])

2.1 Diamond Synthesis via Shock

The formation of small diamond clusters using shock impacts was one of the earlier methods used to reach the high pressure and temperature conditions necessary for the equilibrium formation of the diamond phase. The first reproducibly created diamonds via shock synthesis were made by DeCarli in 1959 when investigating the similarities between radiation damage and shock wave damage on nuclear-grade graphite, with results published in 1961 after rigorous confirmation via XRD performed by Jamieson [16]. Typical experimental setups begin with graphite sheets, which are then subjected to shock pressures of at least 20 GPa [27–29] driven by explosives or gas gun impact [30]. Modern use of lasers to produce shock in graphite precursors has also produced diamond and even the hexagonal diamond, lonsdaleite, at sufficient shock pressures [31]. The shock pressure and associated temperature rise create the stable conditions for diamond to form, but the times that these conditions are held are so small that usually only small clusters of diamond are formed before the system returns to a graphite stable zone. The fast quenching of the diamond is necessary for it to retain its form and not revert to a graphitic phase, and the method of quenching are also capable of producing different morphologies [32–34]. Because of these fast formation time frames, shock synthesis is generally unable to create large diamond samples, and the sizes of the clusters themselves are not tightly controlled either. Figure 3 shows the different *P*-*T* regions for several methods of synthesizing diamond. Shock synthesis uses higher pressures than static methods.

Meteor impacts also can create the conditions necessary for diamonds to form. Many crater impact sites have provided evidence of diamond formation via impact with the earth, such as Canyon Diablo in Arizona [36–39], the Ries crater in southern Germany [40], the Popigai Crater in Russia [41], intact meteorites from Antarctica [42], or the possible origin of carbonado (black diamond) in Brazil and Central Africa [43]. Figure 4 shows a diamond crystal embedded within a meteorite sample from the Canyon Diablo site. While not man-made, the shock produced by the meteor impact produces the conditions necessary for their formation, and several unusual forms of diamond have been found from these impact sites.

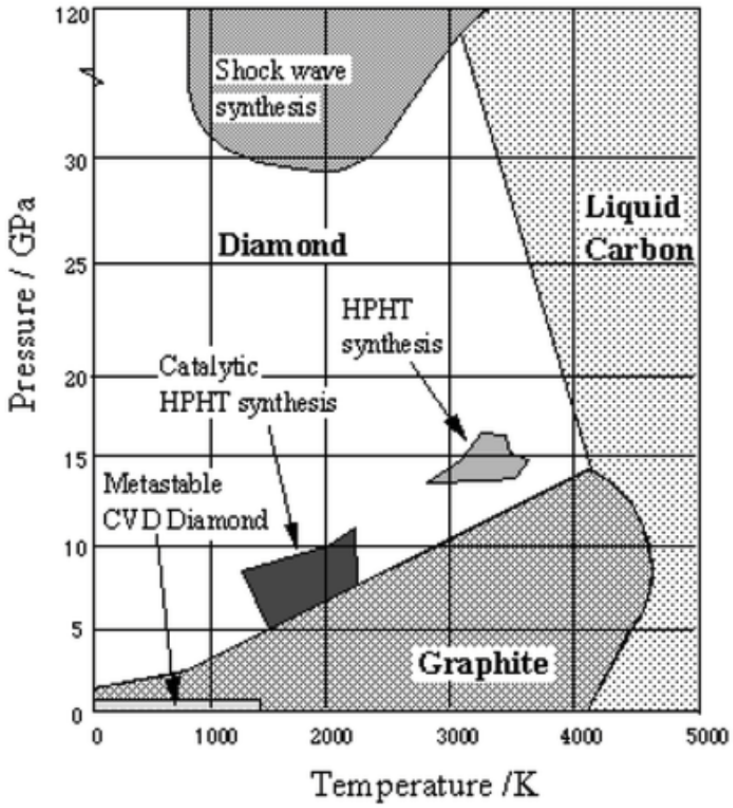

FIG. 3. Phase diagram of carbon showing the temperature and pressure regimes that the various methods for creating diamond are located in. (taken from Ref. [35])

2.2 Diamonds from Detonation of Explosives (Ultra Dispersed Diamonds)

Diamond can also be the product of the detonation itself. These nanosized diamonds (4-7 nm) were found to be 25% of the soot resulting from the detonation of TNT/RDX, TNT/TATB, and TNT/IIGU mixtures, as reported by Greiner et al. [44] in 1988. This work was simultaneously reported in the US and USSR. In the USSR, it was pursued with the recovery of the nanosized diamonds for technological applications. One of them was the mixing of the powders with lubrication oil for automotive engines in order to 'break them in' by smoothing the cylinder bores. Newer technology producing smoother bores rendered this product obsolete. Volkov et al. [45] analyzed the formation of diamond and proposed that it forms at the Chapman-Jouguet pressure (19-35 GPa) and temperature (3500-4400 K). The carbon is

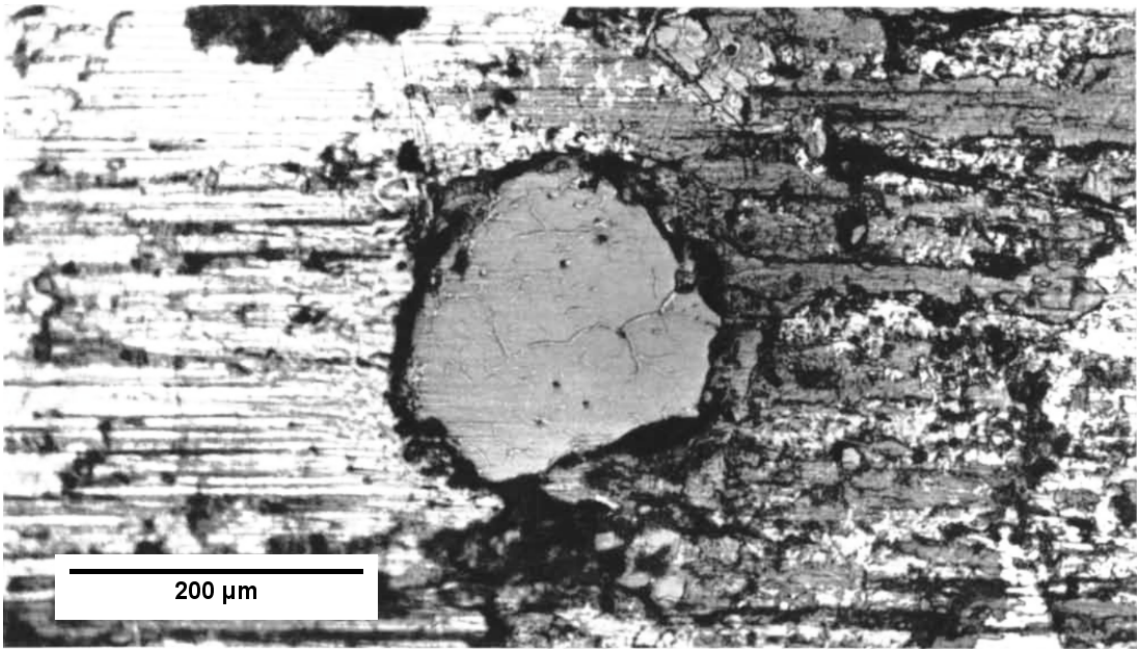

FIG. 4. A diamond fragment embedded within the Canyon Diablo meteorite. Taken from Ref. [37]

produced by the reaction: $2\,CO \longleftrightarrow CO_2 + C$. Carbon is liquid in the Chapman-Jouguet region and therefore liquid droplets are formed, which crystallize upon rapid cooling if conditions are right. Volkov et al. [45] claim that the first experiments forming ultra dispersed diamond date from 1963. Figure 5 shows the Chapman-Jouguet states for a variety of explosives. They are in the liquid region and this explains the formation of nanosized diamond upon solidification.

2.3 Shock Consolidation

Diamond powder with fine particles can be consolidated into a more solid diamond bulk by use of a mechanical means: a shock wave in a process called shock consolidation. This process is more akin to sintering than the formation of diamond from graphite [46]. The important understanding from these experiments are the effects of the diamond particle sizes on how the particles consolidate, as well as the quality of the diamond samples that can be obtained from these methods. Because of diamond's high hardness, pressures of about 100 GPa or above are required for the consolidation process [47], but could

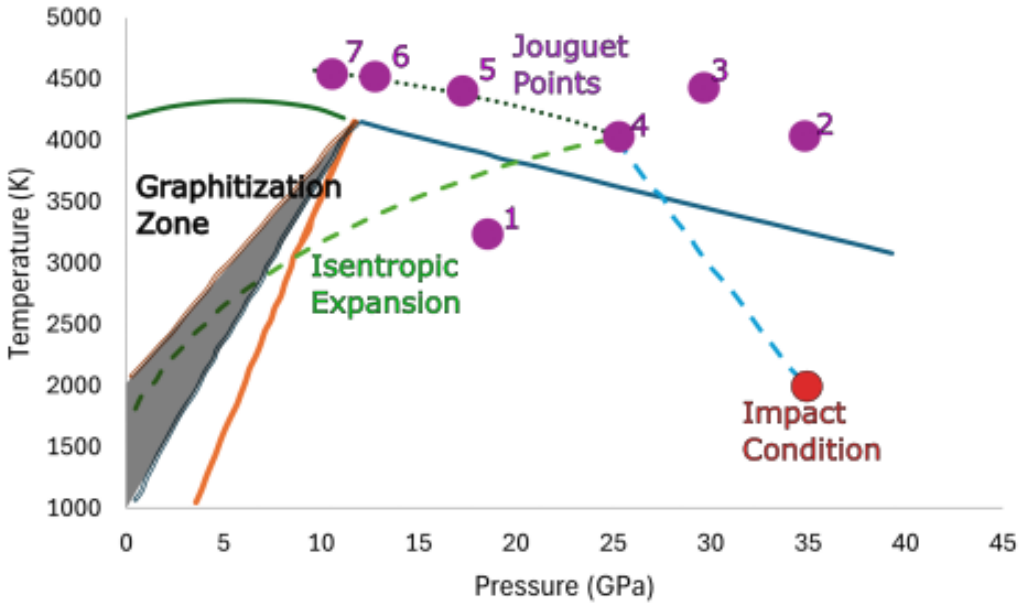

FIG. 5. Pressure vs. temperature diagram for carbon; points 1 to 7 represent Chapman-Jouguet states for different explosives. It can be seen that, except for Explosive 1, the points are in the liquid region. from Volkov [45]

be lowered with the presence of graphite powders added to diamond [48]. However, because of these high pressure shock waves, cracking is also likely in the consolidated samples because of the reflected tensile waves [49]. In general, the density of the consolidated samples can be as high as 90% [50]. Diamond has a natural hardness in the range of 100-150 GPa, and these consolidated samples range from 25 to 80 GPa in hardness [47, 50, 51]. This demonstrates that flaws are present, not allowing the compacts to reach their full strength.

2.4 Presence of Flaws in Diamond

Field and Pickles [52] studied the strength and fracture properties of manufactured diamonds, and showed that they tend to be full of flaws. When compared to natural diamond, manufactured diamonds were on average 3-4 times weaker [9]. Testing of tensile strength in CVD diamond samples, with equivalent flaw size calculated from an assumed K_{Ic} value of 6 MN/m$^{3/2}$, revealed flaw sizes ranging from 40 to 150 micrometers, obtained from a bursting membrane method. The larger the testing area of the dia-

mond, the more likely that larger flaws are present, resulting in lower values of the strength of diamond for larger samples. This is explained by the Weibull analysis whereby the strength decreases with size.

2.5 Brown Diamond

Some of the color in diamonds may be a consequence of the presence of dislocations created by plastic deformation, rather than just the presence of elemental impurities. Both natural and CVD diamonds have been observed with brown coloring. Willems finds evidence of both [101] and [112] type dislocations in brown diamonds [53], and further research showed evidence that small vacancy clusters may affect the coloration as well [54]. There is also evidence that high pressure/high temperature treatment of these brown diamonds can remove this discoloration [55].

3. Static Compression of Diamond

3.1 Diamond Anvil Cell Experiments

Diamond's unique properties led to it becoming the material of choice in the creation of the Diamond Anvil Cell (DAC) in 1959 [56]. By sandwiching other materials between two diamond faces, a very high pressure can be applied to the sample. A gasket is used to keep the material from flowing outwards laterally. Due to diamond's remarkable compressive strength and extreme hardness, it can exert pressures on the sample ranging from tens of gigapascals to even terapascals [57, 58].

Since it is optically transparent, direct microscopic observation of the sample under pressure can be made. Additionally, diamond is transparent to more than just visible light. X-rays are another extremely valuable source of spectroscopic data, and diamond's low atomic number means it has a low absorption. By utilizing the single crystalline nature of the diamonds used in DACs, if the diamond is oriented such that it does not fulfill the Bragg condition, the x-rays also minimally attenuate due to Rayleigh scattering. Infrared, gamma, UV, and even photons also prove that diamond's transparency make it perfect for the purposes of studying other material under high pressure [59, 60]. Figure 6 shows the structure and imaging within a DAC.

When DACs subject other materials to these high pressures, the diamond itself also experiences those

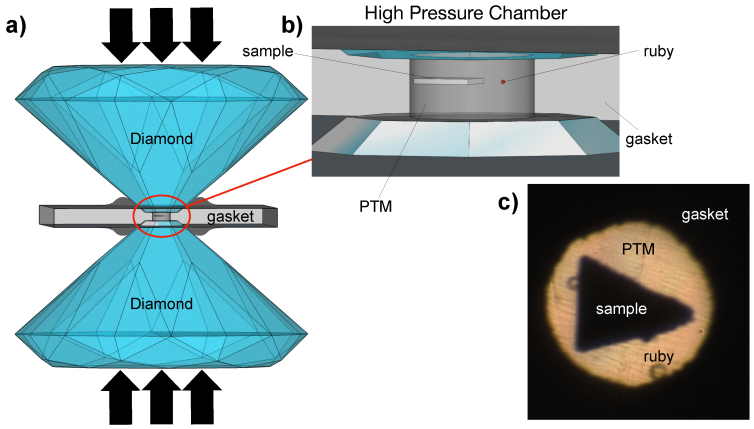

FIG. 6. Schematic and images of a diamond anvil cell. (a) Diagram of the DAC (b) Detail of on the high pressure chamber (c) Real image of the sample chamber within the DAC [61].

pressures. Physical analysis of anvil cells removed after experiments to a pressure of 170 GPa found macroscopic plastic deformation in one of the faces, seemingly dependent on nitrogen platelet concentration [62]. Further experiments studying the response of the diamond itself under these conditions have been performed, observing the deformation of the anvil face up to 400 GPa [63]. A theoretical first-principles study of the non-hydrostatic tetragonal compression present in DACs found that the diamond begins to yield when the shear stress present exceeds 200 GPa, or corresponding to an experimental pressure in the 300 GPa range [64]. These predictions line up with some of the changing properties of the DACs around these conditions, including the fluorescence of the diamond itself as it interferes with commonly used ruby fluorescence [65]. Another study used a moissanite anvil cell capable of pressures up to 500 GPa to study diamond's Raman spectra and the effects of hydrostaticity and nonhydrostaticity in loading [66, 67]. First principles calculations and finite element analysis of diamond and its use in DACs has shown good agreement with experimental results, where properly designed setups with [001] oriented diamond can reach pressures of over 500 GPa, and dual stage nano-twinned diamond can reach up to 1 TPa [68].

3.2 Indentation Testing

Indentation testing of materials is a common method of relatively non-destructive characterization of physical properties. Hardness values are taken by indenting a material with a tip of a specific shape, depending on the type of indentation test being performed. Diamond's place as the hardest natural material makes it perfect for use as the indenter tip, as it can easily penetrate the surface of other softer materials, but issues arise when diamond itself needs to be tested. Since diamond is used to indent diamond, deformation or even failure of the indenter tip can occur. The Vickers and Berkovich indenters are unsuitable to the task as they tend to produce irregular indentations on the testing surface [69]. Use of the shallower Knoop indenter made of high quality single crystalline or nanopolycrstalline diamond has shown the most consistent results but needs to be paired with additional microscopy such as AFM or SEM to accurately measure the size of the indentation [70]. One of the earliest measurements of plasticity in diamond used a Knoop test and, interestingly, found that shear events formed along the (100) planes rather than the (111) planes as expected [71]. A review of diamond indentation hardness by Chaudhri [72] argues that much of the previous data for diamond indentation hardness is incorrect due to these factors, and the true hardness for diamond is likely to lie between 130 and 145 GPa.

Nanoindentation studies on small diamond crystals found a strong orientation dependence in the loading response of diamond. Hardness values of 95 GPa were found for the (100) surface, and 117 for the (111) surface [73]. Nanoindentation characterization of thin diamond films grown on a substrate found that hardness tended to increase with pressure, as the deformation increases the sp3 bonding within the nanocrystalline material [74]. Another study looking at obtaining the Young's modulus from nanoindentation tests found it to be 1090 GPa in the [001] orientation, in fair agreement with literature values [75].

3.3 Diamond Nanopillar Experiments

Nanopillar experiments provide a unique set of conditions for observing plasticity in diamond. Recent advances in nanopillar construction techniques and electrostatic deformation have enabled the study of nanoscale diamond pillars under load. These nanoscale experiments may exhibit very different mechanical properties than their bulk counterparts, but are a means to provide insight into the mechanical

response. Researchers at Zhejiang University used in-situ TEM to perform nanopillar compression experiments on diamond. They were able to directly observe dislocation loops forming at the compression zone and were able to identify that these dislocation loops actually lie on the (100) planes [76, 77]. A different study subjected diamond nanopillars to bending and found that the (111) oriented samples only deform elastically, returning to their original shapes or failing in a brittle fashion, while the (100) oriented samples underwent plastic deformation, and possibly formed a new orthogonal phase with 8 atoms (O8) of carbon under these loads [78]. A further discussion of the nanopillar experiments can be found in Section 8.

4. Diamond Phase Diagram

Figure 7 shows a phase diagram of carbon that is constructed from an early model by Young and Grover [83] as well as several ab initio calculations of the high pressure and temperature phases of diamond [80, 82, 84–86]. Willman's [85] carbon SNAP machine learning potential results are also included. The graphite phase is not shown, but would occupy a sliver of the leftmost portion of the chart, as it is stable only to at most 15 GPa. The shock melting curve can be seen from Eggert's [79] experimental data. The features of most of the phase diagrams are quite similar, apart from the earliest calculations. The transition from diamond cubic to body-centered cubic 8 (BC8) takes place at around 1 TPa. Diamond's melting point increases with pressure until around 400 GPa, where it begins a negative Clapeyron slope. This negative slope is also seen for the transition from diamond cubic to BC8. A simple cubic phase exists above $\sim$2.8 TPa at 0 K; even further beyond the boundaries of Figure 7 hexagonal phases are predicted to be stable. While the BC8 phase is predicted to occur at 1 TPa and above, experimentally it has not been observed [7]. Ab initio predictions of the phase changes of diamond agree with the experimental results as well, with the diamond cubic phase remaining as the metastable state until reaching the threshold for the simple cubic phase to occur at >2 TPa [87, 88]. The kinetic restrictions and high energy barriers between the two phases simply do not allow for diamond to directly transition to the BC8 phase. While some calculations did show that relaxation of the simple cubic phase into the equilibrium

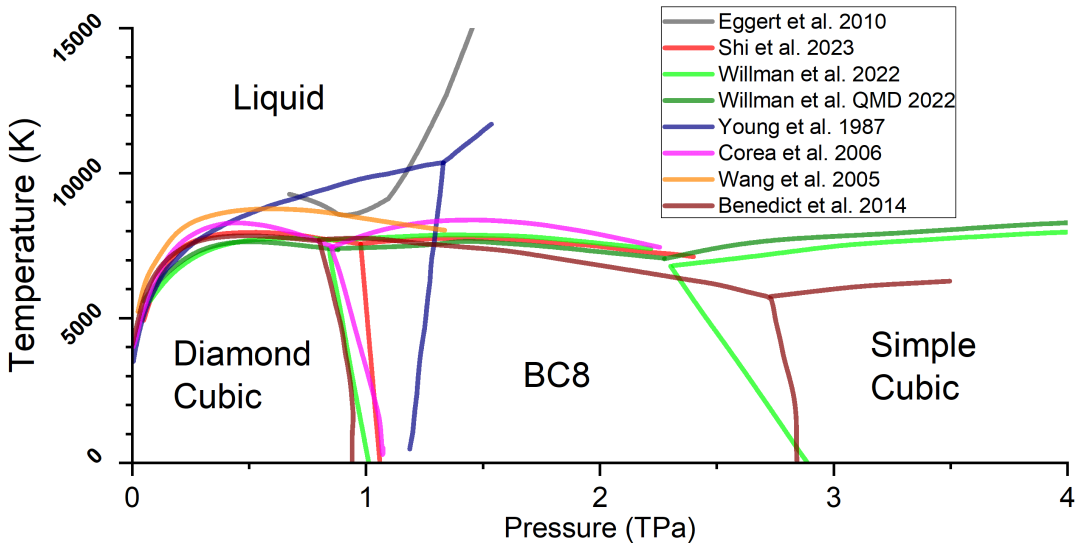

FIG. 7. A phase diagram for diamond up to 4 TPa and 15000 K has been consolidated from several sources, including early first principles estimates of the phase boundaries, up to the most recent machine learned calculations for the phase transitions of diamond. Aside from the earliest calculations performed for the transition from cubic diamond to body-centered cubic 8 (BC8) in 1987, the general features of the different phases tend to line up well. The cubic diamond to BC8 transformation has a negative slope between temperature and pressure, as well as the transition from BC8 to simple cubic at even higher pressures (∼3 TPa). The BC8 to liquid transition begins with a positive slope which then turns downwards. Eggert's experimental data on the diamond Hugoniot also captures a portion of the melt curve, and is in fair agreement with Wang's ab initio calculations. (Ref. [79–84])

BC8 region produces the elusive phase, another pathway for creating it is currently under investigation at the National Ignition Facility of LLNL [3, 84]. By taking metastable nanocrystalline diamond into the BC8 phase but above the extended diamond melt line, a metastable supercooled liquid state is formed. If this liquid state is then cooled and held in the thin BC8 region as seen in Figure 8, the new crystal phase eventually forms.

Hexagonal diamond was initially identified in meteorites [38, 89]. Synthetic hexagonal diamond was later produced in laboratory in 1967 [90]. Hexagonal diamond is composed of tetragonal C-C bonds with similar bond lengths and density as cubic diamond [90]. Hexagonal diamond is believed to be an excellent substitute for cubic diamond due to its potentially excellent mechanical properties. However, the

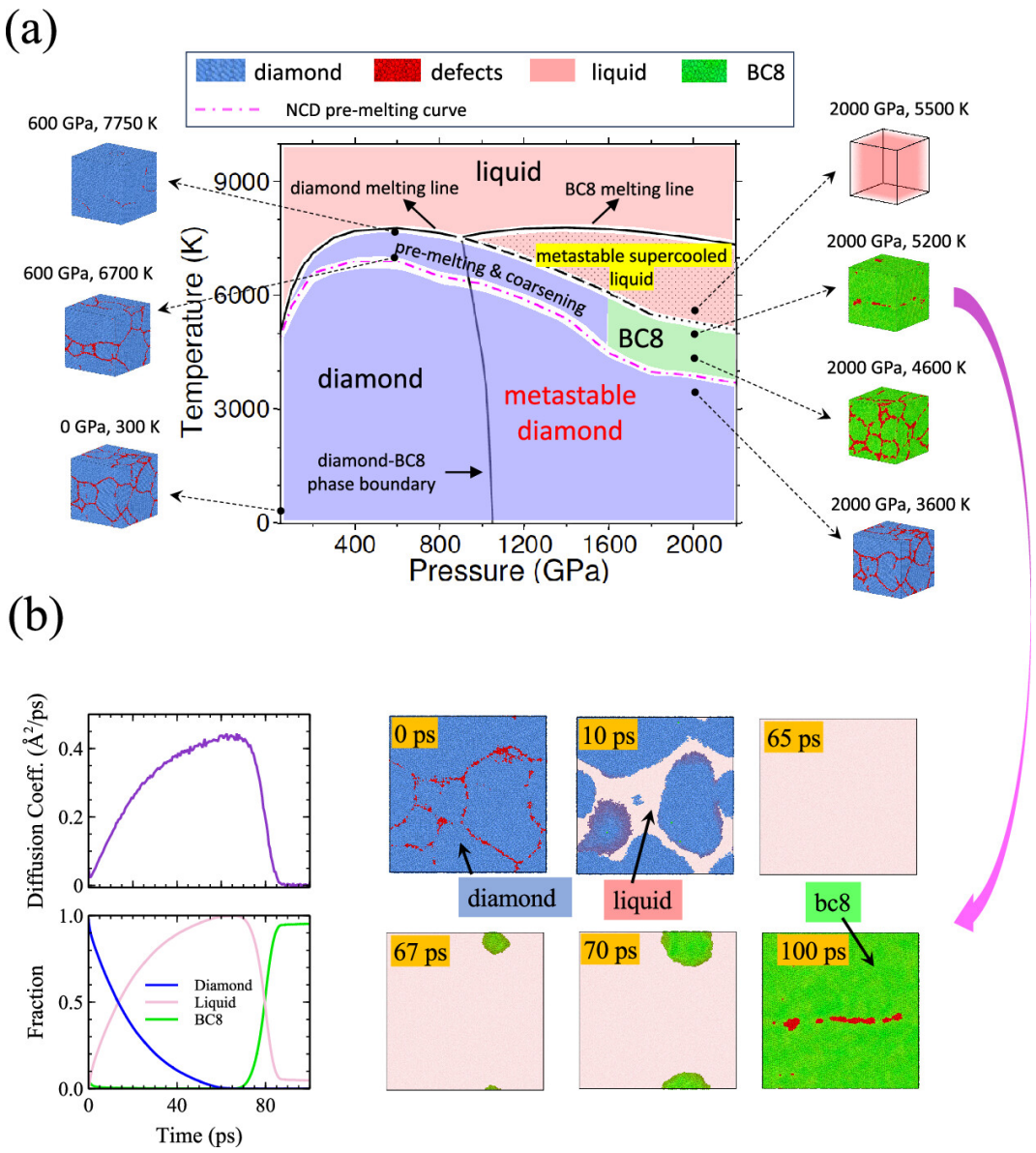

FIG. 8. A possible metastable pathway towards experimentally forming BC8 diamond. a) Shows the extended diamond melting line; if the diamond is taken above this line it will form a metastable supercooled liquid. If the temperature can then be lowered into the green BC8 zone, the BC8 crystal structure should form. b) A time-lapse sequence of the change in diamond simulated when taken from the metastable diamond phase up to the supercooled liquid state, then lowered to the BC8 formation zone. (Ref. [3])

mechanical properties of hexagonal diamond have only been investigated by computational calculations because there are no available macroscopic specimens for experiments [91]. An exception are shock synthesized and meteorite diamonds, which can be hexagonal. Hexagonal diamond is predicted to be stiffer [92], stronger [93], and has larger elastic moduli [94] while thermodynamically less stable compared to cubic diamond by computations. The longitudinal moduli of hexagonal diamond are measured to be much higher than that of shock-formed cubic diamond and even ambient cubic diamond single crystals. The shear moduli of hexagonal diamond are determined to be at least 8%–13% larger than that of cubic diamond. However, this is only a qualitative measure because the bulk modulus is unavailable to be measured [95]. The shear modulus of a defect-free crystal determines the material's strength and hardness [95, 96]. Therefore, the stronger and harder hexagonal diamond is supported over cubic diamond by the experimental evidence although the strength of a crystalline material is determined only from its shear modulus and defect density [97].

5. Molecular Dynamics of Diamond under Extremes

5.1 Molecular Dynamics

Simulating diamond using molecular dynamics or ab initio calculations begins with the ability to model carbon with different bonding configurations. Tersoff developed in 1988 one of the first potentials widely adopted and still in use today Tersoff [98]. It has a simple description for bonding strength based on the number of nearest neighbors, i.e. based on the concept of "bond-order". It is still one of the fastest carbon potentials available and is often used as a benchmark for comparison with other more recent or complex carbon potentials. Further developments in these types of classical potentials have given rise to other ones which may describe well a particular type of carbon behavior. However, in general these potentials fail to capture all aspects of the behavior across the full range of temperatures and pressures, environments, or bonding behaviors, that diamond and carbon can experience. Thus, many studies use molecular dynamics with other classical potentials to study diamond behavior. Especially at the lower end of the high-energy regime, below 200 GPa and under the melting curve, the behavior of these potentials can provide valuable insight into mechanical properties of diamond, such as dislocations, stacking-fault energies, tensile or yield strengths, and others. Modifications of parameters such as bonding cutoff lengths, bond angle strengths, and attractive pair potential, are common in attempts to improve the performance of the Tersoff potential for different ranges of pressure or temperature. Each of these potentials endeavors to describe particular system conditions, such as graphite interlayer interactions, hydrocarbons, and metal-carbon alloy interactions.

5.1.1. Tersoff Potential

As mentioned above, Tersoff's [98] is still one of most widely used classical interatomic potentials; it was originally developed for silicon and later adapted to silicon carbide, while also describing the pure carbon-carbon bonds. Previous 3-body attempts to describe silicon had proven unsatisfactory for the range of bonding geometries and coordination numbers, and increasing the number of bodies considered introduced too many variables to the problem. Tersoff [98] decided to implement the physics of the

problem directly into the equations, where the bond order determined bond strength, being influenced by neighbor geometries and coordination. The formulation of the potential simply summed the energy of each bond,

$$E_{ij} = \sum_i E_i = \frac{1}{2} \sum_{i,j \neq i} V_{ij} \tag{1}$$

where

$$V_{ij} = f_c(r_{ij})[A \exp(-\lambda_1 r_{ij}) - B_{ij} \exp(-\lambda_2 r_{ij})] \tag{2}$$

The A term describes repulsive forces, as seen in other two-body potentials. The B term describes bonding forces, including bond order and local environment. Any considerations for bond angles, competing bonds, and bond strengths are folded into this variable. This equation is further expanded upon by Tersoff's parameterization seen in the trial potential B_{ij}, which includes measures for the number of competing bonds, how their strength falls with increasing coordination, ratio of bond strengths, angle between bonds. f_c is the cutoff function, which limits the range at which atoms will interact with each other, substantially reducing the computational load.

Several different variants of the Tersoff potential exist with just slight tweaks to the parameters or the functional form used [99]. There are many versions of the Tersoff potential with simply adjusted cutoff distances that improve performance in a variety of pressure environments [100, 101]. An alternative version for high pressure was recently presented [102]. The Tersoff potential describes physical properties of diamond with good agreement to both experimental data and first principles calculations. Cohesive energies, bond lengths, elastic properties, and point defect properties all are within reasonable error.

Studies of mechanical deformation of diamond using the Tersoff potential show dislocation plasticity, in good agreement with experiments. This includes studies on defective single crystals [103], polycrystals [104, 105], and nanoparticles [106, 107]. Experiments for loading along [111] also show dislocations gliding on {100} planes, instead of the more usual {111} planes, and Tersoff is also able to reproduce that [103]. Studies of dislocations and plasticity using the Tersoff potential have shown good agreement with

some of more unique properties of diamond, such as its dislocations along the (100) planes [103, 106]. An image of these type of dislocations emanating from a void can be seen in Figure 9. Li et al. [103] subjected monocrystalline diamond to shock compression along three orientations ($[100], [011], [111]$), and obtained results that are surprising; the $[100]$ orientation did not yield defects even past the Hugoniot elastic limit, up to a pressure of 130 GPa, while the $[111]$ orientation in Figure 9 exhibited dislocation generation starting from the surface at even lower pressures. The insertion of a void magnified the emission of dislocations because of the stress concentration effect. Both $[110]$ and $[112]$ type Burgers vector dislocations formed on the (001) and (111) planes respectively. Whereas the former have been found to be present in plastically deformed diamond [71, 76], the latter are novel. The computational results found are consistent with nanopillar deformation along the same 3 orientations [76].

5.1.2. Other Potentials

There are many potentials developed for C. Two open online repositories are the ones at NIST (https://www.ctcms.nist.gov/potentials/system/C/), OpenKim (https://openkim.org/browse/models/by-species#C), and in the database at http://carbonpotentials.org/potentials. A few of the most popular potentials are detailed below.

The Erhart-Albe potential [108] is a modified Tersoff potential fitted for silicon, carbon, and silicon carbide. Compared to previous potentials, it describes elastic properties even better, and demonstrates transferability across regimes by simulating condensation of silicon-carbide in an inert gas environment. It has been used often in conjunction with the Tersoff potential to corroborate results in nanotwinned diamond [109].

The Stillinger-Weber potential [110] was originally created for silicon and other tetrahedrally bonded crystals. The first parametrization for carbon was created in 1991 [111] and improved with increased interaction length including second nearest neighbors in 2002 [112, 113]. The potential explicitly defines the energetic contribution of triplets of atoms, and penalizes deviation from the tetrahedral angle. It found most use in simulations involving other materials also using a SW potential, such as water and silicon.

The Brenner potential, also known as the REBO potential, is based on Tersoff's covalent-bonding

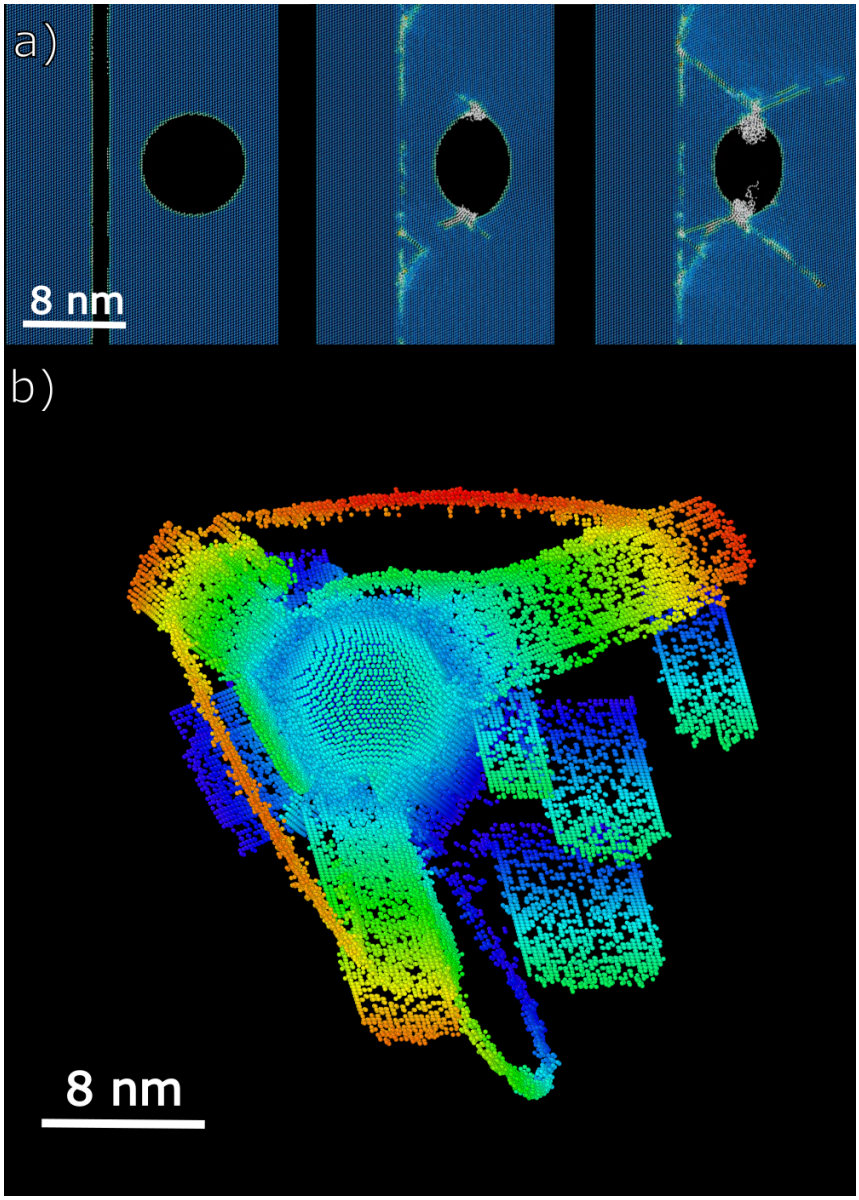

FIG. 9. a) 2-d slice of the [111] loading orientation simulation with a void and dislocations emitted from both surface and the void at a pressure of 137 GPa. b) Rectangular 1/2[110](001) dislocations can be seen emanating from the 8 nm diameter void in this molecular dynamics simulation of shock through single crystalline diamond, along with half-loop dislocations along the (111) planes. From [103].

formalism with additional terms that correct for an inherent overbinding of radicals and that includes

nonlocal effects [114]. It has been used to study shocks in diamond [115] and diamond melting [116]. There are many extensions to the Brenner model, including versions to improve both short-range and long-range interactions [117].

The Adaptive Intermolecular Reactive Empirical Bond Order (AIREBO) potential was another potential [118] originally created for hydrocarbons, which improves the description over the previous REBO potential by including torsion, dispersion, and non-bonded repulsion interactions, making possible a more realistic simulation of graphitic systems. Repulsive and attractive terms are combined with a proportional bonding term in the Tersoff style, with repulsive terms in the Brenner style. M-AIREBO improves the short term interactions to simulate systems at moderate pressures [119].

The carbon MEAM potential [120] is based on the embedded atom potential. It attempts to describe both the structures of carbon while providing the ability to describe metals and metallic interactions. This allowed it to be extended for use in alloyed metal-carbon systems [121].

Another type of potential was formulated based on Tight Binding model [122–124] and fitted against DFT calculations to capture the quantum mechanical nature of covalent bonding in carbon. While this potential has been of most interest in the simulations of other carbon materials such as nanotubes [125, 126], there have also been some applications for studying diamond [127].

The Environment Dependent Interaction Potential [128] is better fitted to liquid and amorphous carbon phases, with superior performance to Tersoff and Brenner in these areas. Buchan used this potential to study radiation damage cascades within diamond [129], and it is particularly apt to describe amorphous carbon hybridization versus density, and its mechanical response [130].

The original reactive force field potential [131] was created with bond-order considered specifically for modeling interactions including chemical reactions. Modifications of the ReaxFF C-2013 potential [132, 133] were made from a previous potential developed for hydrocarbons. Fitting parameters for the potential were obtained from equations of state for graphite and diamond calculated via DFT. This potential is actively used for simulations involving systems with multiple species which might involve chemical reaction.

For the Long-range Carbon Bond Order Potential (LCBOP) potential [134, 135], short-range interac-

TABLE 1. Classical Potentials for Carbon and their uses

Potential	Year	Type	Notes
Tersoff [98]	1986	Bond Order	Elastic constants, defects
Erhart-Albe [108]	2005	Bond Order	SiC in inert gas
Stillinger-Weber [110]	1985	Three-Body	Combined with silicon, water
Brenner [114]	1990	Bond Order	Melting
AIREBO [118]	2000	Bond Order	Hydrocarbons
MEAM [120]	2005	Embedded Atom	Metal-carbon alloys
Tight Binding [122–124]	1992-1995	Tight-Binding	Nanotubes, amorphous carbon
EDIP [128]	2002	Environmentally Dependent	Liquid and amorphous
ReaxFF [131, 132]	2008	Reactive Force Field	Chemical reactions
LCBOP [134, 135]	2003	Bond Order	Includes long-range interactions for things like interplanar graphite binding. Captures diamond graphite transition

tions are described by bond order, while also including long-range interactions for non-nearest neighbors. Short range interactions are based on the Brenner potential. Ghiringelli [136] used this potential to create a very accurate graphite-diamond melt curve and triple point prediction.

Table 1 summarizes some of the properties and uses of the different potentials.

5.1.3. Machine Learning Interatomic Potentials

Machine learning and interatomic potentials derived from it have quickly evolved in the past decade as the new frontier for large yet still nearly quantum accurate simulations. This new type of potentials use machine learning algorithms to train on quantum mechanical data, for instance creating environmental descriptor for the energies and forces that can match the accuracy of the quantum simulations with orders of magnitude less computational load [137–139]. A recent review on Machine Learning potentials [140] lists several for carbon, including one using active learning by Oganov and coworkers [141].

One of the earliest types of machine learning potentials developed was the Gaussian Approximation Potential (GAP) [142]. It uses Gaussian Process Regression (GPR) based on kernels, similarity measurements between the environments of the atoms, and estimates the local energy based on these kernel descriptions [143]. In this way, the non-linear potential energy of the atoms is rewritten as a linear func-

tion in the kernels. There are no assumptions made regarding the physics underlying the data, and is instead a purely statistical representation of the data. There are many GAP potentials for carbon, including the "GAP-20" potential [144], and another version for nanoporous carbon [145].

One of the major difference between the different types of machine learning potentials is how the relationships between the atoms and their energies is described. The Spectral Neighbor Analysis Potential (SNAP) is very similar to GAP potentials, but assumes a direct linear relationship between the atom energies and their bispectrum components [146]. A carbon SNAP potential developed by Willman et al.[85], with focus on the high temperature and high pressure phase changes of diamond, has been used to run simulations with billions of atoms on nanosecond timescales [147]. The propagation of a 4.5 MBar shock wave through diamond can be seen in Figure 10. The shock wave moves from left to right. A fascinating observation is the spatially periodic arrangement of shear bands at $\sim$45°to the shock front. The shear stresses are relaxed by the formation of these bands. Amorphization and possible melting is reported within these bands, and the shocked material could be considered as nanocrystalline, in contrast with the initial monocrystalline diamond. This potential has also been used for predicting and designing experiments which may be able to reach the BC8 phase by employing two consecutive shocks [3]. An extensive evaluation of the potential under extreme conditions displays excellent agreement with benchmark ab-initio results for perfect crystals [148]. This includes uniaxial compression simulations, which are relevant to mechanical properties under extreme conditions. A comparison with several empirical potential is shown, excluding the Tersoff potential which is the one that has been shown to reproduce elastic constants reasonably well up to nearly 200 GPa [106].

Many other machine learning potentials that have been developed for the description of carbon and diamond. Some involve Neural Network (NN) based potentials [149–152], including neuroevolution potentials (NEP) [153, 154] and dropout neural network potentials [155]. There are also atomic-cluster expansion potentials (ACE) [156] for diamond, Chebyshev Interaction Model for Efficient Simulation (ChIMES) [157, 158] and other methods such as moment tensor potentials (MTP) [159] that may be applied as well. ML methods may also be used to help fit more "standard" potentials, like the Tersoff potential [160], which have been applied to C [161]. There is constant advancement in the training

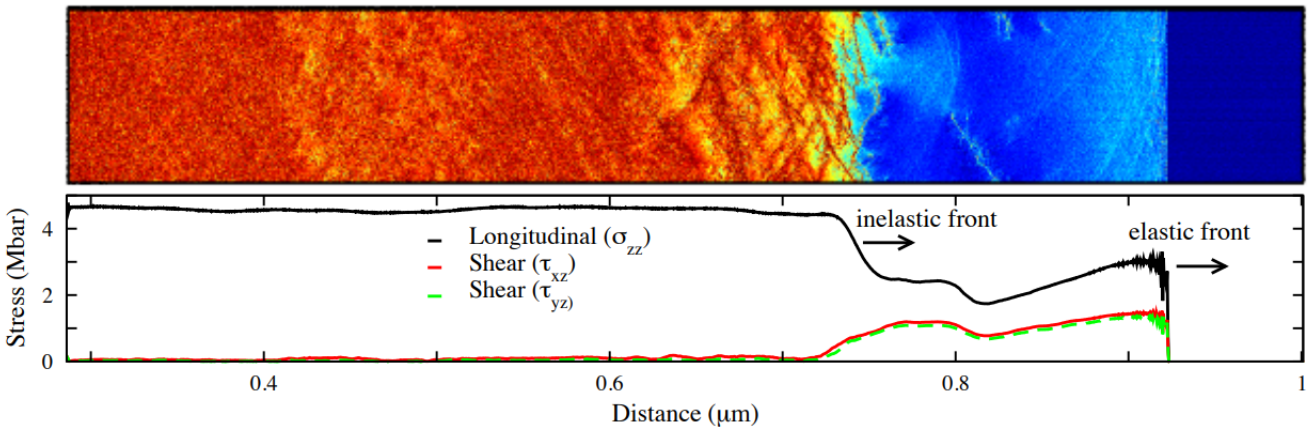

FIG. 10. Shock-wave propagation into diamond (blue) simulated using an Spectral Neighbor Analysis Potential (SNAP) [147]. The shocked crystal contains over a billion atoms and is oriented along the $< 110 >$ direction, being driven at 7 km/s. The elastic wave is followed by a second inelastic wave, colored red, displaying stress relaxation within the brittle diamond through shear bands and amorphization.

methods, such as automated selection of training points [162]. Recently, DeepMD potentials [152, 163] were used to study diamond amorphization [164], and C under warm-dense matter conditions [165], while a NN potential was employed to study the graphite-to-diamond transformation under shocks [166].

It is important to note that machine learning is notoriously unreliable in its ability to extrapolate to points outside of the dataset it was trained on [167]. This means that things not included within the data, such as rare events of diffusion or chemical reactions, or the absence of data for things like defects and dislocations, may result in these machine learned potentials being unable to recreate these phenomena. Especially in the case of extreme conditions, these machine learned potentials must be properly vetted to ensure their transferability and accuracy for the many different features of diamond. Liu *et al.*[168] highlight the need to include a variety of point-defect configurations in the ML training, something that most ML pots for C do not consider. In addition to isolated point defects, dislocations are extended defects which have been observed in diamond at high pressures using both experiments [169] and simulations [103]. However, we are not aware of any ML potentials for C including extended defects configurations in their training, unlike what has been done for several metals, where dislocations and

stacking faults are sometimes included [139].

Another important issue is the computational performance of ML potentials compared to conventional potentials. Earlier versions took up to few 1e3 times more than "standard potentials [160, 170]. However, many steps have been taken to achieve a reasonable performance, allowing the simulation of large samples. This includes possibilities to run in GPUs [153, 154], and it has also been explored for fast implementation of SNAP [148] and DeepMD [171] potentials. One of the challenges with the efficiency of any potential is the range of the interactions. At ambient conditions, potentials like Tersoff [172] include only nearest neighbors, while EDIP [128] has a coordination-dependent range. This becomes a more serious concern when the training of ML potentials is required [173], and some ML implementations only include nearest neighbors to save computational cost. GPUMD includes up to 3^{rd} nearest neighbor for many of its potentials [154].

6. Ab Initio Molecular Dynamics

While classical (empirical) potentials-based molecular dynamics is useful to simulate and study large systems, comprising millions of atoms, they heavily rely on fitted parameters that must be calibrated to experimental data to reproduce specific thermodynamic or elastic properties of the material. But even when these parameters have been calibrated properly, their reliability becomes uncertain when extrapolated to thermodynamic conditions that are significantly different from those at which they were fitted, resulting in a possible failure to describe matter under extreme conditions. Classical potentials often fail to accurately predict the transition to a new solid phase under high pressure, or they may substantially underestimate (or overestimate) the melting temperature as a function of pressure. For instance, the Tersoff, Stillinger-Weber, and Embedded Atom Models described in Section 5 fail to describe carbon phases properly [174], have provided a poor description of amorphous carbon [128], and have significantly overestimated its melting temperature at high pressure [175]. More sophisticated potentials, including the AIREBO potential [118], enhance the depiction of carbon structures by incorporating van der Waals interactions, but even the most intricate empirical potentials fail to provide an accurate portrayal of all

relevant properties of diamond. In such scenarios, especially when experimental data is scarce, turning to quantum mechanics becomes imperative.

Although inherently more computationally demanding, quantum mechanics offers the advantage of providing precise descriptions of materials at arbitrary conditions without relying on experimental feedback. *Ab initio* (quantum mechanics-based) simulations enable the exploration of phenomena beyond the limitations of classical potentials, offering unparalleled insights into the electronic structure, bonding behavior, and dynamic properties of solids and liquids under extreme pressures and temperatures.

Molecular Dynamics based on *ab initio* calculations (AIMD) is a powerful computational method that combines the principles of quantum mechanics with classical molecular dynamics simulations. In AIMD, the atoms are subject to forces that are derived from solving the electronic structure from density functional theory (DFT). This approach considers the electronic wave functions and the nuclear positions as coupled variables, allowing for an accurate description of electron-ion interactions and quantum effects. Once the quantum-mechanical problem is solved for the system of static atoms and the ground state of the system is found, the forces derived quantum mechanically are used to move the atoms classically, using Newton's equations of motion. The electronic excitations are incorporated through the Mermin functional [176]. Thus, while the method is based on quantum mechanics, it is not equivalent to quantum molecular dynamics (QMD), because the nuclei are still treated as classical particles. AIMD offers new insights into the electronic structure, bonding behavior, and dynamic properties of solid and liquids subjected to, in principle, any pressures and temperature.

As we have discussed in Section 4, diamond exhibits very particular properties under extreme conditions of pressure and temperature, including extreme metastability across hundreds of GPa of pressure [3, 7], remarkable strength [177], and a transition to a metallic phase upon melting [178]. AIMD simulations provide detailed insights into these phenomena by explicitly considering the changes in the electronic structure and, hence, the nature of the bonds between carbon atoms. In addition, *ab initio* techniques allow for the computation of nuclear quantum effects such as zero-point energy, which is not included in MD, electron delocalization, and electronic excitations. Performing AIMD simulations for diamond under extreme conditions requires advanced computational techniques and high-performance

computing resources. Efficient algorithms, parallelization strategies, and quantum mechanics packages are essential for accurately capturing the quantum behavior of diamond at the atomic scale. AIMD simulations can shed light on various aspects of diamond behavior under extreme conditions, including phase stabilities, lattice dynamics, electronic properties, and defect formation. By elucidating the underlying mechanisms governing diamond's response to high pressures and temperatures, AIMD can contribute to a deeper understanding of its behavior in diverse scientific and technological contexts.

Efforts to obtain the phase diagram of diamond at high pressure through *ab initio* simulations are numerous [82, 86, 179–182]. Correa *et al.* [86] used density functional theory (DFT) to implement two-phase simulations of solid and liquid carbon to determine the solid/liquid coexistence line and free energy calculations to obtain the Diamond/BC8 phase boundary. Similarly, Benedict *et al.* [82] combined path integral Monte Carlo with DFT simulations to generate a multi-phase equation of state for carbon from a model based on the free energies obtained. Both studies find two local maxima on the melting curve and a transition from the Diamond phase to the BC8 phase around 1000 GPa at 0 K. While *ab initio* simulations have provided a much better description of carbon at high pressure and remarkable agreement with experiments, inconsistencies with experimental data still exists [82].

Diamond compression beyond the pressures feasible with static diamond anvil cells has been possible thanks to shock compression. However, the significant heating induced by shocks leads to sample melting before pressures can reach 1 TPa. Only with the relatively recent advent of the ramp compression technique [6, 7] has it become feasible to explore the terapascal regime of solid diamond. Recent efforts to model ramp compression via AIMD have provided crucial insights into the behavior of materials under extreme conditions, particularly focusing on high-pressure states well below those induced by shock Hugoniot compression curve. The study by González-Cataldo et al. [181], provided a framework to model ramp compression experiments through AIMD, with simulations that were conducted to characterize the response of carbon subjected to high pressures at temperatures, markedly lower than those encountered during shock compression. However, one of the challenges in interpreting ramp compression experiments lies in the uncertainty surrounding the extent of heating that occurs under these shock-free conditions, as direct temperature measurements are typically unavailable or involve large uncertainties.

To address this challenge, González-Cataldo et al. [181] undertook a series of ab initio simulations on carbon, aiming to reconcile the density-stress measurements obtained by Smith et al. [183] Their simulations encompassed a range of scenarios, including isotropic and uniaxially compressed solid carbon in diamond and BC8 phases, with and without defects, as well as simulations of liquid carbon. Their modeling approach postulated that heating during ramp compression originates from the transformation of an initially uniaxially compressed cell into an isotropically compressed state with lower internal energy, thus conserving energy while raising the temperature, as seen in Figure 11. Different loading paths show how the temperature evolution with pressure is dependent on the number of steps. Figure 11b highlights the radically different paths that shock and isentropic compression take. Remarkably, their simulations revealed that multiple such heating events can occur during a single ramp experiment, resulting in higher temperatures than those observed with isentropic compression.

Comparison of the simulation results with experimental data yielded intriguing insights. While heating alone could not fully account for the equation of state measurements on diamond, suggesting the persistence of a significant uniaxial stress component at high compression, their findings underscored the complexity of the compression process. Notably, their simulations suggested that a substantial portion of the deposited shock energy was converted into heat, potentially hinting at the onset of melting, although recent x-ray diffraction measurements provided evidence to the contrary. [7]

Furthermore, González-Cataldo et al. [181] shed light on the inherent challenges in measuring temperature during ramp compression experiments, emphasizing the need for improved techniques to obtain reliable temperature data. They proposed a multi-step model to characterize the effects of plastic deformation and defect generation during ramp compression, offering a promising avenue for future research. Despite the inherent complexities, their study represents a significant step towards understanding the behavior of materials under extreme conditions, with implications ranging from planetary interiors to high-pressure experiments and beyond.

Validating AIMD results against experimental observations is crucial for assessing the reliability and predictive capabilities of quantum mechanical simulations and comparisons with spectroscopic measurements, X-ray diffraction data, and other experimental techniques help validate theoretical models and

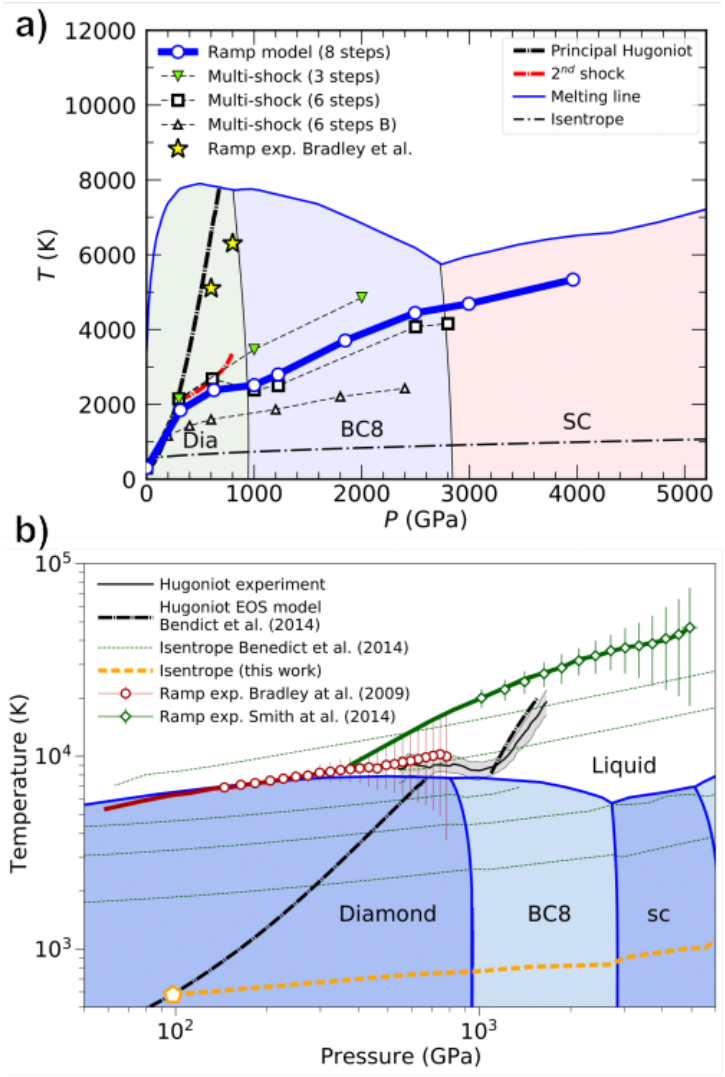

FIG. 11. (a) Linear temperature vs. pressure plot predicted for the shock (Hugoniot), multi-shock schemes, and ramp (quasi-isentropic) loading. Intermediate steps are performed at 1000 and 3000 GPa, where solid/solid phase transitions are predicted to occur. All uniaxial compressions from 1000 to 4000 GPa were performed in the BC8 structure. The melting curve (thin blue curve) [82] is shown for comparison. The dot-dashed black curve represents the isentrope that crosses the principal Hugoniot curve at 110 GPa, the diamond elastic limit. Temperature estimates, based on plastic work, at 600 and 800 GPa from the ramp compression experiments of Bradley *et al.* [4] are shown as yellow stars; (b) Logarithmic plot of temperature vs. pressure showing shock (black curve) and ramped (quasi-isentropic) heating (yellow dashed curve).

refine simulation parameters. Future research directions include the development of hybrid quantum-classical methods, improved treatment of electronic correlations, and integration with experimental techniques for real-time validation and feedback.

7. Monte Carlo Simulations

Classical molecular dynamics modeling is limited in the timescales it can reproduce, but Monte Carlo (MC) simulations can help with the study of equilibrium configurations that might be difficult to achieve within MD timescales. Kinetic MC (KMC), a related technique, can be used for the time evolution of certain systems, provided the rates for the process of interest are known.

KMC has been used to simulate the growth of diamond being produced via chemical vapor deposition [184, 185]. Atomic level definition is given as the vapor deposition growth is simulated with one reaction occurring at each step, with statistically variable time increments between each one. Different reaction species [186], gaseous environments, and other environmental factors can affect the growth rates of diamond. As CVD is one of the most common methods of producing diamond, these studies are important for the optimization of the CVD process. With modern computing power, more complicated geometries and factors can be included in these simulations [187] , as well as multiscale combinations of molecular dynamics and Monte Carlo for ultrafine particle growth [188]. Path Integral Monte Carlo has also been applied with success to cross-validate against ab-initio MD and create a coherent equation-of-state for carbon from ambient conditions to its plasma limit [189].

8. Diamond Experiments Performed under High Energy Density Conditions

8.1 High Energy Density Physics Conditions and Planetary Interiors

High Energy Density Physics (HEDP) is a new field within the domain of condensed matter and radiation physics, where energy densities are sufficiently high such that conventional methods in chemistry and

physics are inadequate to explain the behavior of matter. The HEDP regime is often defined by pressures exceeding 1 megabar, or 100 GPa. Such conditions exist in the interiors of planets and stars [190, 191]. In our solar system, large quantities of carbon are likely be stored in the ice giant planets Uranus and Neptune [192] even though the composition of their interiors is poorly constrained. Since these planets formed beyond the ice line, one assumes that massive amounts of the planetary ices, H_2O, CH_4, and NH_3 were incorporated into their mantles during formation. In the seminal paper [193], M. Ross proposed that methane decomposes into diamond and hydrogen at the high pressure conditions in the interiors of ice giants. The hypothesis of diamond formation has since again further support by results from diamond anvil cell experiments [194, 195], shock measurements [196] and computer simulations [197]. Mercury has recently been added to the list of carbon harboring planets. Based on measurements by NASA's MESSENGER spacecraft, a diamond layer has been proposed to exist on top of the Mercury's iron core [2].

Carbon-rich exoplanets are likely to exist in our galaxy as long as they formed out of a nebula that had a carbon-to-oxygen ratio greater than 0.8 [198]. In these environments, there is not enough oxygen available to form the typical magnesium silicates like $MgSiO_3$ or MgO that make up the bulk of the Earth's mantle. In such cases, the mantles of planets are predicted to be composed of diamond and silicon carbide [199]. *Cancri 55 e* was initially assumed to be such a diamond planet [200] but a more careful analysis of stellar spectra have called into question whether *Cancri 55 e* formed in a carbon rich environment [201]. Instead it has been suggested to be a rocky planet with an atmosphere that is rich in CO and CO_2 [202].

Diamond transforms into graphite before melting at ambient pressure due to its thermodynamically unstable nature. The melting temperature of carbon under pressures of 0.6–1.1 TPa is probed by shock compression experiments on diamond. The melting curve has a negative Clapeyron slope, indicating that diamond melts to a denser, metallic fluid between 0.60 and 1.05 TPa, which agrees well with the first-principles calculation predictions. Diamond melts to a complex fluid at even higher pressures, and dissociates at pressures between 1.1 and 2.5 TPa when the temperatures are above 50,000 K.

Because of diamond's strength [203–205], a variety of extreme techniques such as gas guns, explo-

TABLE 2. HEL for Single Crystal Diamond

Authors	Year	<100> (GPa)	<110> (GPa)	<111> (GPa)
McWilliams et al. [177]	2010	80	81	60
Kondo et al. [207]	1983	110	63 ± 28	
Lang et al. [220]	2013	53 - 93.9	62.1 – 86.9	62 – 87.2

sives, and pulsed lasers have to be used to allow it to reach the realm of temperature and pressure that may be defined as High Energy Density. Shock Hugoniot data of diamond from many sources is presented in Figure 12 [177, 178, 203, 204, 206–217]. The experimental results are very consistent up to 1 TPa; beyond that there is considerable scatter in data.

8.2 Diamond Hugoniot Elastic Limit and Strength

The Hugoniot elastic limit (HEL) is an essential property of materials under high strain rate shock compression. Below the HEL, the material is under uniaxial compression condition without permanent deformation; at HEL, solids undergo the highest shear stress under shock compression; above HEL the shear stress decreases and relaxes to hydrostatic compression condition, plastic deformation and material failure initiate [218]. This dissipation of stress is generally achieved in three forms: ductile-like by plastic flow, brittle by fracture, or phase transformation through atomic rearrangement [219]. The uniaxial strain state above the HEL has hydrostatic (isotropic) and deviatoric (anisotropic) stressed components; and the deviatoric component is a function of the strength of the material [211]. The HEL and strength measurements largely depend on the types, growth methods, density, and grain size of diamond samples used in experiments. Different initial imperfections in diamond can lead to a discrepancy of 10% - 20% on the measured values for HEL and strength. Table 2 presents HEL values for three orientations of single crystals diamond [177, 207, 220].

Single crystal diamond was shocked by plate impact experiments to about 900 GPa elastic impact stress (EIS, the stress obtained at impact, assuming purely elastic diamond response) to explore the elastic-inelastic response of [100], [110], and [111] orientations by Winey et al. [210]. A two-wave structure (elastic-inelastic response) was observed at ∼900 GPa EIS at or near the melting stress along [110] and [111] directions while single (overdriven) waves were observed at 480 GPa EIS and above

along [100]. The elastic wave velocities along [110] and [111] were much larger than those along [100]. The elastic wave amplitudes along [110] were much larger than those along [100] and [111]. And along [110] and [111], the elastic wave amplitudes rose significantly with increasing EIS, indicating strong orientation dependence. The two-wave structure and the large orientation dependence nature of elastic wave speeds and amplitudes illustrate that the response of single crystal diamond is not hydrodynamic up to shock stresses below the onset of melt [210].

The strength and nonlinear elastic response of natural and synthetic (type IIa) single crystal diamond were also measured by Lang et al. [204] through plane shock wave experiments of 60 ns duration along [100] direction to peak elastic pressures of 90 and 120 GPa. The maximum elastic wave amplitudes for both crystals are 89 ± 3 GPa, corresponding to shear stresses of 30 GPa for $(111)[1\bar{1}0]$ and 35 GPa ($\sim G/15$) for the $(111)[2\bar{1}\bar{1}]$ slip system. Under the higher peak stress, the elastic limit of 57 GPa was unexpectedly lower. The elastic constant C_{111} was determined to be -7804 ± 653 GPa. Particle velocity histories showed a sharp elastic wave which was followed by a second wave. Compression to stresses just above the HEL is linked to the formation of a two-wave shock structure, characterized by an elastic precursor propagating at a longitudinal sound speed which compresses the diamond to near its HEL and is followed by an inelastic wave which reaches the peak pressure. This two-wave structure is characteristic of a material which has a time-dependent, elastic-inelastic response.

Lang et al. [205] also explored the elastic-inelastic response of shocked single crystal diamond, including how crystalline anisotropy affects the elastic limit, strength, and deformation by plate impact experiments to ∼120 GPa along [110] and [111] directions. Their HEL values are given in Table 2. Understanding and quantifying the strength or elastic limit of diamond single crystals is significant for science and technology. The elastic limits exhibit highly orientational dependence under uniaxial strain conditions. The maximum resolved shear stress (MRSS) values reach the maximum ($\tau_{\max} \sim$ G/15) along the [110] and [100] orientations and minimum ($\tau_{\max} \sim$ G/20) along the [111] orientation, showing significant orientational dependence. The MRSS values calculated for the [110] and [100] directions correspond to 25% – 30% of the calculated theoretical shear strength for {111}<110> slip systems in perfect single crystal diamond. The MRSS values depend strongly on the resolved normal stress which is the

stress component normal to the {111} slip planes, explaining the orientational dependence of strength in shocked single crystal diamond: [110] > [100] > [111]. The results show that the resolved normal stress can suppress the initiation of inelastic deformation in shocked single crystal diamond. The lower elastic wave amplitudes at higher shock stresses and the impact of stress normal to the slip planes indicate a highly time-dependent inelastic response which is typical in shocked brittle solids, rather than the dislocation slip mechanisms [205, 221–223].

Single-crystal diamond bridges, approximately 1 μm in length and 100 nm in width, were microfabricated and tested by Dang et al. [224]. These samples exhibited extremely large (sample wide), reversible, and uniform elastic strain deformation through in situ uniaxial mechanical tensile tests along the [100], [101], and [111] orientations at room temperature. A maximum tensile strain of up to 9.7%, approaching the ideal elastic limit [8], was achieved. The Young's modulus was measured to be around 1010 ± 70 GPa in the [111] direction, which is higher than the values of ∼895 ± 65 GPa and ∼850 ± 80 GPa for the [101] and [100] directions, respectively. These results are consistent with the expected ranking of orientation-dependent elastic moduli for bulk diamond [225, 226].

The strength of laser shocked polycrystalline diamond at stresses above the HEL was examined by x-ray diffraction with velocity interferometry at the Linac Coherent Light Source. Typically, brittle materials lose considerable strength above the elastic limit [227]; shocked diamond exhibits a unique elastic–inelastic response [177]. Both ramp compression [4, 6] and shock compression at [204, 205] and above [177] the HEL were conducted to probe the dynamic behavior of diamond. Diamond behaves in a brittle manner at ambient conditions like most materials with high initial strength, but it has a plastic response under shock compression condition [177]. The experimental results show that shock compressed diamond retains ∼ 20 GPa of strength at 150 – 300 GPa longitudinal stresses, which gives valuable data for developing improved strength models of diamond. These models will promote simulations in inertial confinement fusion implosions and reduce the uncertainties in EOS [211].

8.3 Shock Compression

Shock-wave experiments up to 191 GPa and 217 GPa were conducted along the intermediate direction between <111> and <110> on diamond by Kondo et al. [207] (HEL measurements in Table 2). The highest post-shock density from about 200 GPa shock compression was 3.95 g/cm^3 while its initial density was 3.52 g/cm^3, indicating a transformation to a denser metallic carbon phase induced by shock or an elastic unloading process. The post-shock diamond metallic carbon phase is stable at the lower mantle and earth core, which is of geophysical interest [206, 207].

Cubic diamond is the strongest naturally occurring material, and is thermodynamically stable over a wide pressure and temperature range. At 172 GPa, a macroscopic flow similar to plastic deformation was observed at the tip of a diamond anvil at above 2000 K by Mao et al. [228]. Cubic diamond transformed to graphite when a sharp diamond indenter was pressed on its surface [229]. Cubic diamond particles directly transformed into hexagonal diamond under shock compression in nanoseconds at only tens of GPa and hundreds of K, thermodynamically still within the stable cubic diamond phase domain. The transformation from cubic to hexagonal diamond is a kinetic solid-to-solid transition induced by shear stress and the increasing temperature generated by shock compression. Cubic diamond has the "*ABCABC*..." stacking sequence of identically packed carbon layers, while hexagonal diamond has the "*ABAB*..." stacking sequence. High shear stress is generated during shock compression due to the high stiffness of diamond under the uniaxial strain condition. The shear stress may induce stacking faults or multiple twin intersections, resulting in a transition of stacking faults from the "ABC" to the "AB" sequence. At the Hugoniot elastic limit (HEL), solids undergo the highest shear stress under shock compression; exceeding this, the shear stress decreases and plastic deformation initiates. The best shock pressure to produce hexagonal diamond is ∼70–80 GPa, which is about the HEL of cubic diamond (see Table 2), corresponding to a shear stress of around 30 GPa. This enhances the explanation of the importance of shear stress. High shear stresses combined with the temperature rise promote the formation of hexagonal diamond with shear stress. If the shear stress is high enough but the temperature is not high enough to form hexagonal diamond, cubic diamond transforms to disordered graphitic carbon. If the

temperature is too high, it may lead to the graphitization of hexagonal diamond. Appropriate temperatures are required for the formation of hexagonal from cubic diamond, and approximately 500 K is favorable [230].

Decades of experiments show that the diamond–liquid melting line has a positive slope above the graphite–diamond–liquid triple point [231]. Theoretically, the melting curve of diamond should have a maximum at a higher pressure [80, 81, 232, 233], because the sp^3 hybridization loses its stability in the fluid phase. High-pressure measurements conducted using laser shock along the diamond shock Hugoniot indicate that crystalline diamond likely melts into a conducting fluid. The shocked diamond starts to melt at about 750 GPa. A negative volume discontinuity is observed at melting, indicating it has a negative melting slope at a maximum at 300–500 GPa on the melting curve. The presence of this maximum is due to the coordination change from two- and threefold at low pressure to tetrahedral in the fluid [234]. This change is due to the stabilization of diamond-like bonding at elevated pressures. But because the diamond-like bonding destabilizes, it becomes a more condensed fluid [80, 86, 214, 232]. This behavior is akin to silicon on melting, which also exhibits a negative Clapeyron slope. Si and C have the same covalent bonding configuration and crystal structure.

Magnetically accelerated flyer-plate experments on diamond were conducted at the Sandia Z machine [235] from 550 to 1400 GPa. There is evidence of a diamond-bc8-liquid triple point at the melting boundary. Under high pressure and density condition of the planet's ice layer, the free carbon may condense as diamond. Diamond is used as an ablator material for inertial confinement fusion capsules. In the high energy density carbon phase diagram, the first slope change at 700 GPa pressure and 6.08 g/cm^3 density corresponds to the onset of melting of the diamond phase. The second slope change at pressures and densities between $\sim$850 to 880 GPa and $\sim$6.53 to 6.67 g/cm^3 corresponds to a triple point along the solid melting boundary. The third slope change at 1064 GPa and 7.01 g/cm^3 corresponds to the end of melting of a solid phase other than diamond. These values correlate well with the ab initio molecular dynamics (AIMD) simulations predictions for the triple point at 850 GPa and 6.52 to 6.62 g/cm^3 and for the onset and end of melting at $\sim$680 GPa and $\sim$1040 GPa, respectively [212].

The two-wave shock structure containing elastic and inelastic compression wave was discovered in

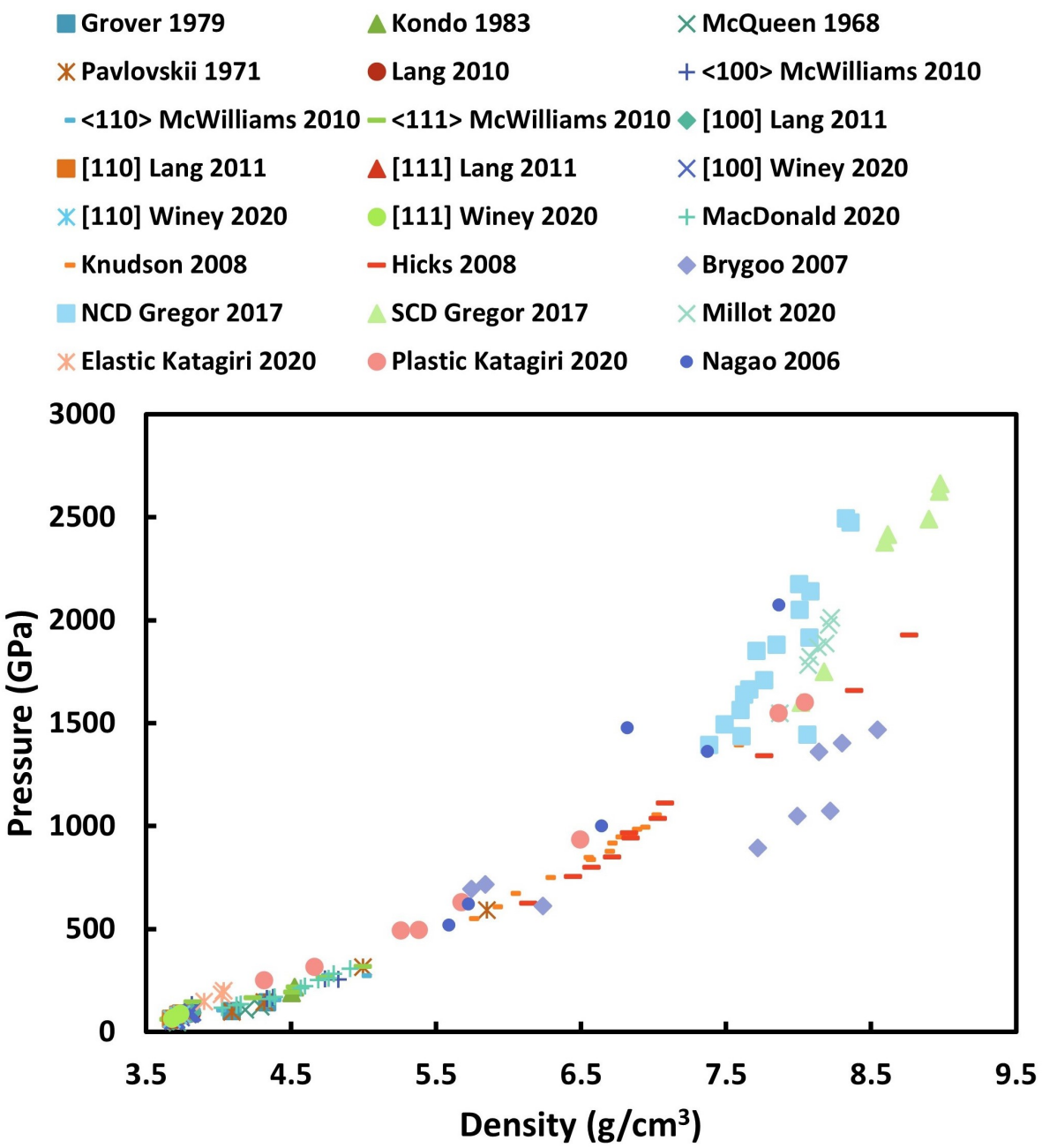

FIG. 12. Diamond shock Hugoniot experimental data from different sources [177, 178, 203, 204, 206, 207, 209–217, 236]

laser shock compression on single crystal and polycrystalline diamond up to 800 GPa. The yield strength of single crystal diamond is about 1/3 of the theoretical predictions. The measurements demonstrate evident deviations from an elastic-plastic response following dynamic yielding, showing substantial relaxation to an isotropic stress state of at least 160 GPa. Features of melting at 700–800 GPa along the diamond Hugoniot may correlate to the shift from a two-wave to a single-wave structure, which supports the explanation that the onset of melting occurs at lower stresses, around 600 GPa, coinciding with the occurrence of a carbon phase with optical reflection. The yielding behavior of single crystal and polycrystalline diamond is measured by large-amplitude shock waves between 100 and 1000 GPa. Although diamond resists plastic flow and tends to yield by fracturing at ambient pressure and temperature [237], plastic flow has been detected under high pressures [238] and temperatures [237], albeit over considerably longer time scales than those investigated through shock compression. The diamond shock response varies from nearly elastic isotropic to nearly elastic-plastic, depending on initial sample properties. While the onset of melting implies that strength should not have an influence in this stress regime, the observations suggest that this is not accurate. Ramp-wave response reveals that solid diamond maintains considerable strength to ramp stresses up to 800 GPa [4], suggesting that it can play a similar role in shock compression experiments [177].

Shock compression on single crystal diamond along the [100], [110], and [111] orientations was used to determine its nonlinear elastic response to 120 GPa peak elastic stresses. The complete set of third order elastic constants is shown in Table 3 combining theoretical models, experimental data, and ab initio simulations at 0 K. Third-order elastic constants exhibit the lowest-order anharmonic and anisotropic response of a crystal, which quantify the nonlinear elastic response of a solid. Anharmonicity plays a significant part in initiating solid to solid phase transformations [203].

Hard x-ray free-electron lasers (XFELs) pulses were employed to investigate the evolution of an elastic wave in diamond with both high spatial (about 500 nm) and temporal (about 50 fs pulse duration) resolution. The elastic wave was generated by an intense optical laser pulse and imaged at various delay times. Figure 13 shows the phase-contrast images captured at 1.2 to 3.0 ns time delays, illustrating the decay of the elastic compression wave with the 3 ns duration. The contrast diminished at the longer time

delays. Moreover, even though the front width of the elastic compression wave was atomic, the direct observation of the propagation of the front width for a material under shock pressures above HEL would lead to better understanding of the time scales involved in plastic flow under high strain-rate conditions above 10^9 s^{-1} [239].

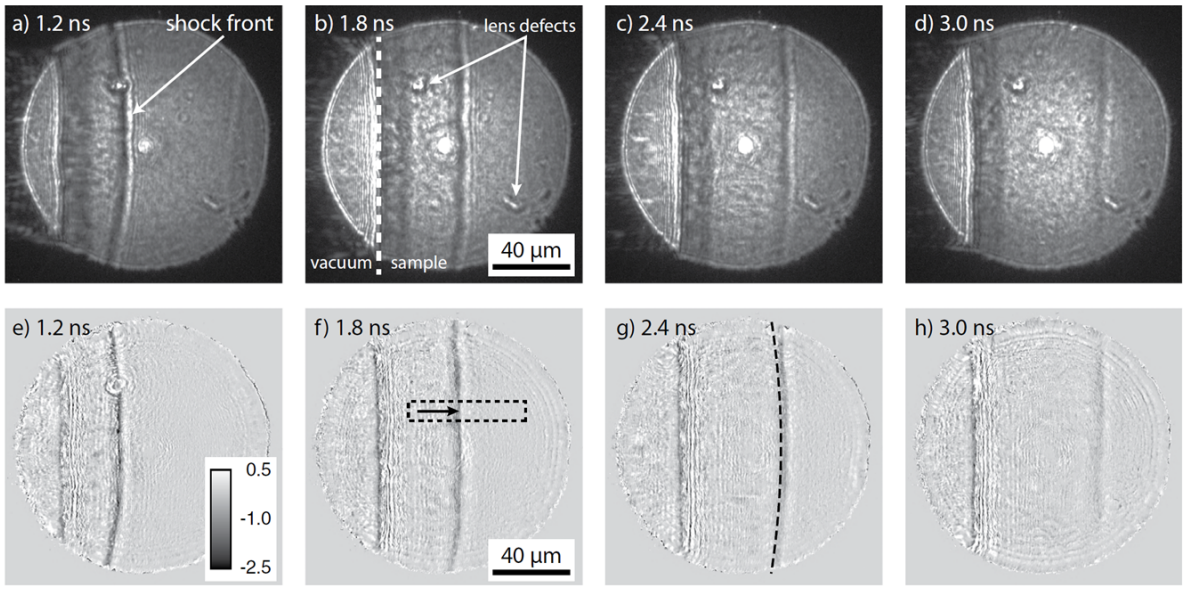

FIG. 13. (a–d) Phase contrast images acquired from 4214 mm behind the specimen by a high-resolution x-ray detector marked by corresponding time delays. (e–h) Corresponding phase maps from iterative phase retrieval. (inset in Fig. e) Gray values illustrate the phase shift radians. The rectangular box in (f) can infer the compression of material [239].

The optical properties of single crystal diamond along <100> direction were examined by shock compression experiments from 60 to 550 GPa. Diamond can retain its transparency during both compression and the subsequent release process when the applied stress is below HEL. The transparency limit of diamond at 532 nm is about 170 GPa according to the experimental results. However, between HEL and the transparency limit pressure, diamond is transparent only in the compression process. McWilliams [177] reports HELs for diamond varying from 60 GPa (for [111]) to 80 GPa (for [100]). It loses its transparency gradually during the release process following shock. The refractive index of single crys-

tal diamond along <100> is observed to increase as density increases to the transparency limit, while in static compression experiments the refractive index decreases when pressure increases up to 40 GPa [240]. The significance of these optical properties is for developing diamond as the premier material for shock impedance windows in velocity measurements during dynamic compression experiments. When the shock pressure in diamond is below 170 GPa, diamond is transparent, which enables it to be used as an optical window. The shock compression state of a material can be explored by the density dependence of the diamond refractive index using a diamond window. Above 170 GPa, the formation and growth of defects lead to polycrystallization during the compression process, making diamond opaque in the early shock propagation stage. There are distinct differences between the polycrystallization process of diamond under shock compression below and above 170 GPa [241].

High pressures are believed to induce methane pyrolysis, resulting in the separation of carbon and potential formation of a diamond or metallic layer. The response of multi-layered diamond at pressures 300-900 GPa was studied by laser-driven planar shock compression under extreme high pressure and temperature conditions. The experimental results by Jakubowska et al. [245] show that a reflecting state of the material was generated by the shock propagation, which agrees well with 1D radiative hydrodynamic simulations using different EOS for diamond. No significant changes in shock velocity were observed although the shock pressure is not retained over time due to the short duration of the laser pulse. This reflecting state of diamond is due to electrons being thermally excited into the conduction band. These quasi-free electrons exhibit plasma-like behavior and can reflect the probe beam when the density is higher than the critical density associated with the VISAR laser wavelength [245].

As mentioned in Section 8.2, the HEL is an essential measure of material strength under high strain rate shock compression [218]. As mentioned earlier, when subjected to a high amplitude shock stress higher than the elastic limit, the material transitions from a one-dimensional elastic deformation to a three-dimensional plastic deformation to rapidly dissipate shear stress [246]. The mechanical properties of a fine-grained polycrystalline bulk diamond differ significantly from those of a single crystal, in spite of being the same material [247, 248]. The same phenomenon is characteristic of metals and is expressed through the Hall-Petch relationship. Bulk nanopolycrystalline diamond (NPD) has been reported to have

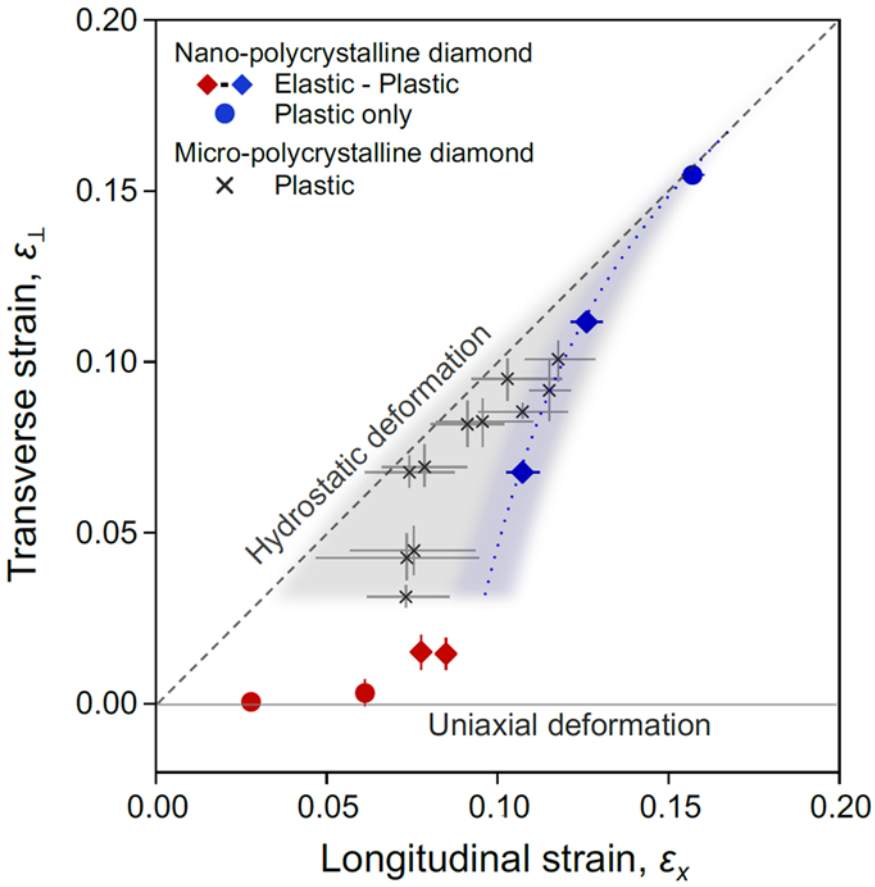

FIG. 14. Evolution of transverse and longitudinal strains in diamond under shock compression. Purely elastic and plastic responses of shocked NPD are marked by red and blue circles, respectively. Continuous elastic-plastic deformations of NPD are marked by red and blue diamonds. Plastic deformation responses of MPD are marked by black crosses [211, 242]. Blue and grey shaded areas and the blue dotted curve indicate NPD and MPD are different [243].

the highest Vickers hardness [249] and HEL [216] of all diamonds. It is essential to know how nanograins deform under high strain rate compression for developing high-strength materials and their applications under extreme conditions. The laser shocked nano-grain reinforced polycrystalline diamond experiments were conducted using *in-situ* femtosecond XRD using an x-ray free electron laser (XFEL) beam [250] to understand its dynamic elastic-plastic transition deformation processes and strength evolution. Shock

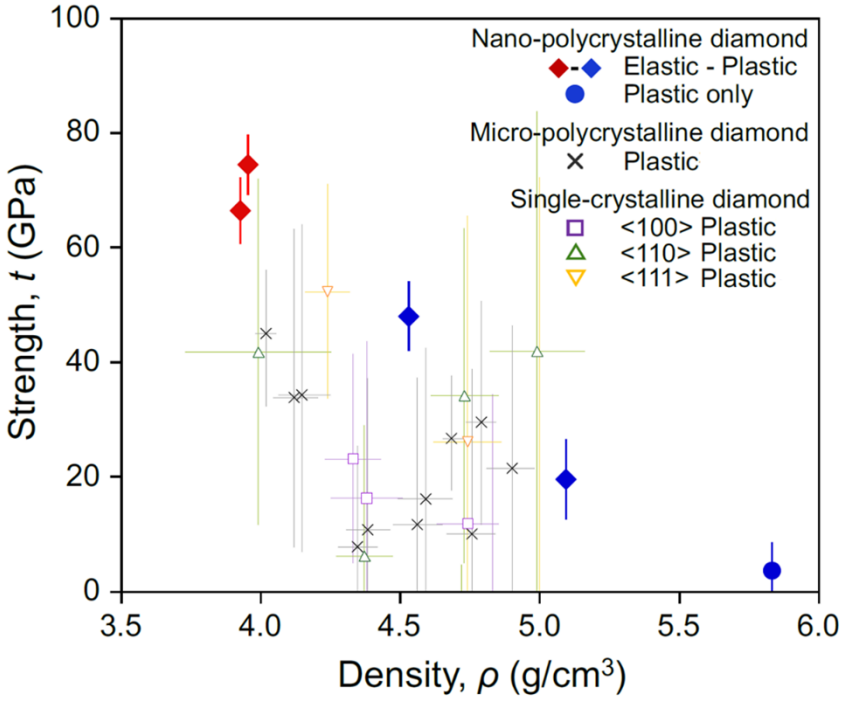

FIG. 15. Strength of shock compressed diamond. The responses of single crystal diamond along three different directions are marked by open symbols: <100> (purple square), <110> (green triangle), and <111> (yellow reverse triangle) [177]. Other colored symbols are identical as in Fig. 15 [243].

compressed NPD with an average grain size of 10-20 nm [249] is ideal to study how materials reinforced by grains lose their strength. Grain boundary strengthening is believed to play an important role because the strength of shock compressed NPD is larger than that of single crystal and micro polycrystalline diamond (MPD). Under shock compression, some brittle materials lose their strength immediately after the pressure exceeds the HEL [227, 251], while others have a brittle-ductile behavior [252]. Whether diamond behaves brittlely or ductilely under shock compression is largely unknown [177, 211]. However, NPD exhibits some ductility by showing considerable strength at applied stresses much higher than HEL until it finally reaches zero at $\sim$700 GPa from XRD experimental results. Figure 14 shows transverse and longitudinal strains measured from the diffractions from (111) planes of shocked NPD and compares them with MPD [211, 242]. Whereas MPD tracks the strain in hydrostatic compression, NPD shows a

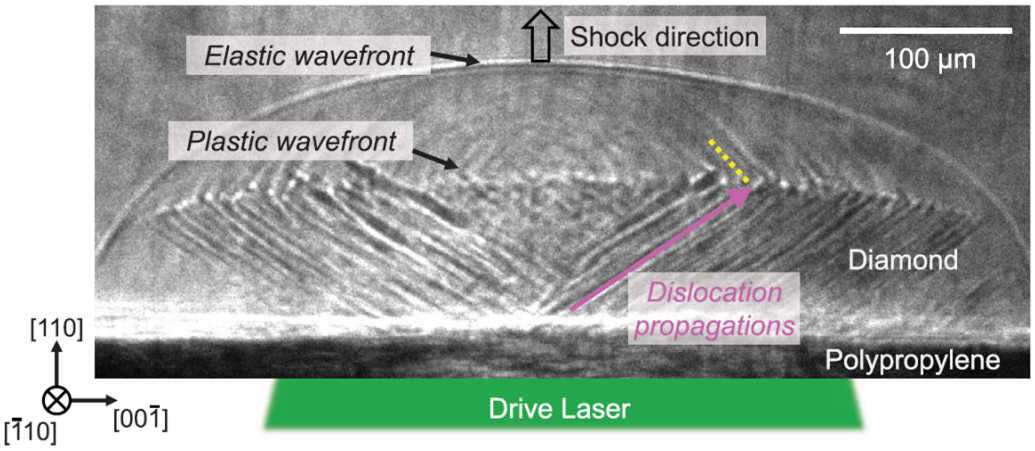

FIG. 16. Femtosecond x-ray radiography image of diamond under shock compression. The elastic-plastic shock wavefronts travel in the shock direction. Dark and bright bands behind the plastic wavefront are stacking faults defined by partial dislocations propagating with plastic shock wavefront marked by the magenta arrow. The yellow dotted line highlights the phonon radiation [169].

considerably higher longitudinal than transverse strains. The ability of a material under high pressure to accommodate local shear stresses in different directions determines its brittle or ductile response. Figure 15 shows the strengths of shock compressed NPD, MPD [211, 242], and single crystal diamond [177]. The strength of NPD under shock compression in the volume deformed plastically is retained until the plastic wave exceeds the elastic wave, producing a single shock wave which instantly compresses the material to the peak pressure. These conditions of overtaking suggest that the strength observed in the volume deformed plastically at lower pressures could be a remnant of the strength present in the prior volume deformed elastically. Even a strong material like diamond loses its strength so quickly that the original lattice transitions into complex dynamics under dynamical high pressure compression [243].

8.4 Dislocation Velocities in Extreme Deformation

Dislocation motion has been studied for over 60 years, but their maximum velocity is still unknown. Speed limits are suggested by models and simulations for dislocation motion, in the subsonic to transonic boundary, where the dislocation self-energy diverges. Nevertheless, these models do not exclude the

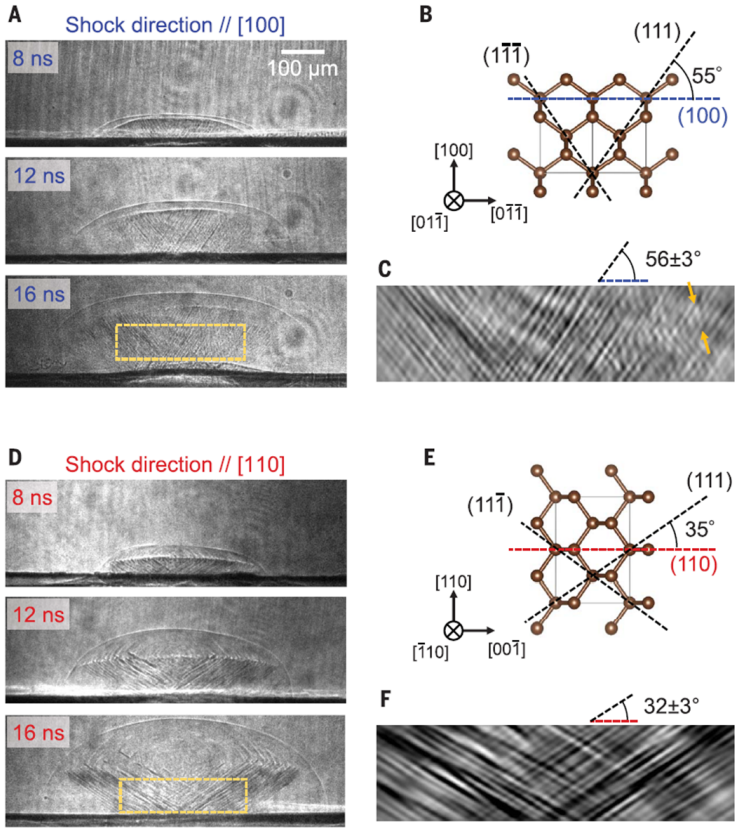

FIG. 17. Illustration of stacking faults in shock compressed diamond. (A) X-ray radiography images of [100] shock orientation. The corresponding XFEL probe delay to the laser irradiation is marked on each image. (B) Lattice of diamond without distortion marked by corresponding plane orientations [244]. (C) Fast Fourier transform (FFT)–filtered image of stacking faults corresponding to the region marked by the yellow dashed rectangle at 16 ns in (A). The orange arrows highlight one of the bands nonparallel to 111 planes. (D) X-ray radiography images of [110] shock orientation. (E) Lattice of diamond without distortion exhibiting the plane orientations. (F) FFT-filtered image of diamond shocked along [110] direction at 16 ns [169].

potential occurrence of transonic dislocations. There is a second barrier in the transonic-supersonic boundary. The ultrafast dislocation movement in single crystal diamond generated by shock compression was tracked by femtosecond x-ray radiography [169, 253]. The leading edges of partial dislocations move transonically as evidenced by the observation of stacking faults extending at speeds exceeding the slowest sound speed. It is important to understand the maximum mobility of dislocations in crystals

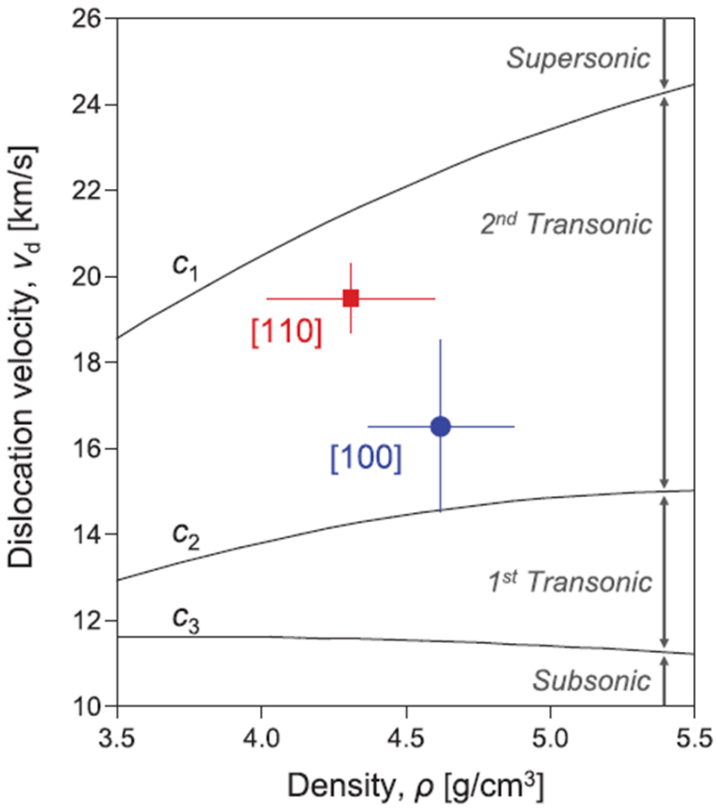

FIG. 18. Calculated and experimentally determined dislocation velocity v_d and longitudinal and transverse sound speeds (c_1, c_2, and c_3) of [110] diamond versus the density. [169].

for precise modeling, prediction, and manipulation of their mechanical properties, particularly under extreme conditions [254, 255]. High strain-rate sensitivity is exhibited by many materials [256] even though dislocation-mediated plasticity is insensitive to the strain rate in some cases [257].

Materials deform by dislocation motion at near sound speed under the highest strain rates. Theoretical dislocation models suggest that the self-energy and dislocation stress diverge when a dislocation travels near the threshold velocities within a specific crystal [258–261], indicating that dislocations are forbidden to move beyond the limiting speeds. While the limiting speeds for dislocations are the same as the transverse and longitudinal sound speeds in isotropic single crystals [262, 263], they are on the same order of magnitude but not exactly the same for the anisotropic single crystals like diamond. Many

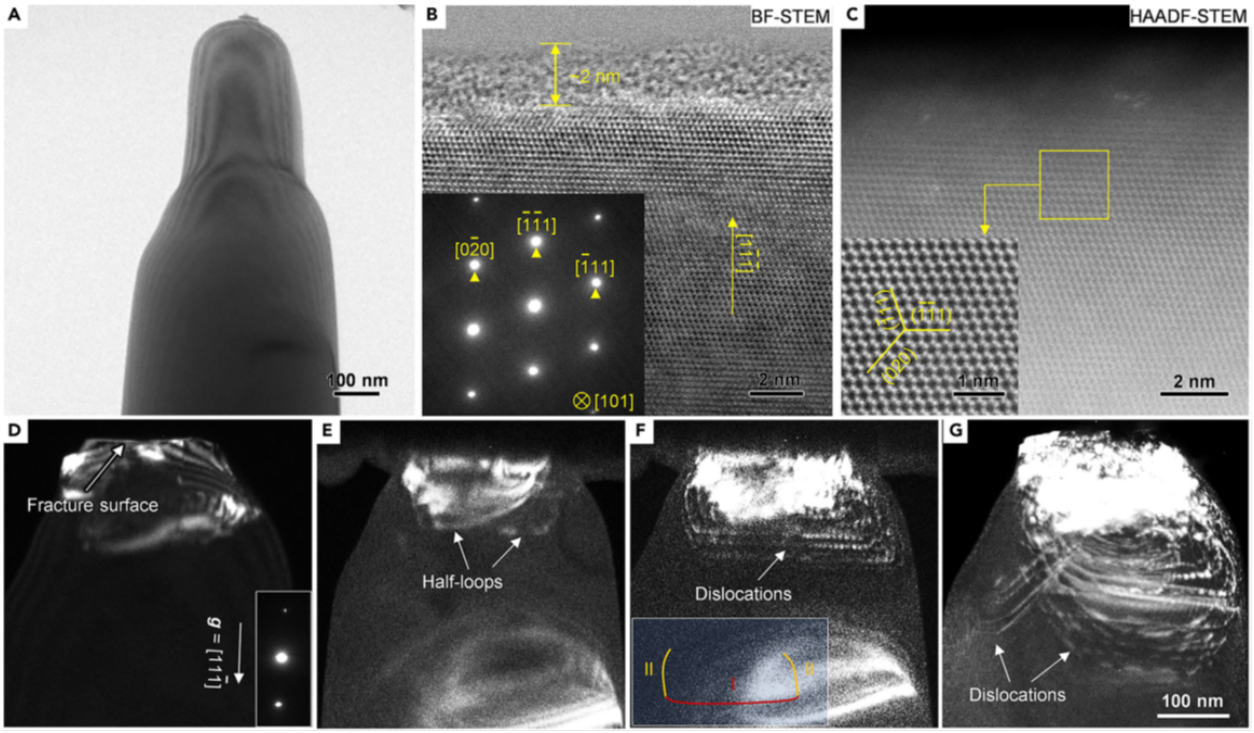

FIG. 19. TEM images of a diamond nanopillar compressed along [111] direction. (A) Bright field image of a diamond nanopillar prior to compression test. (B) Atomic resolution bright field image. Inset of (B) is a selected area electron diffraction (SAED) pattern. (C) High-angle annular dark-field scanning TEM (HAADF-STEM) images. Inset of (C) is magnified atomic resolution HAADF image. (D)Weak-beam dark field TEM image of the diamond nanopillar after the thinner head of the nanopillar partially fractured from the thicker shoulder owing to stress concentration. (E) Dislocation half-loops originated from the fracture surface under compression. (F) Dislocation half-loops multiplied and propagated. Inset of (F) indicates half-loops with the head segment marked by red (I) and arm segment by orange (II). (G) Dislocations activated in multiple planes [76].

theoretical models and MD simulations have demonstrated transonic or supersonic dislocation motion, suggesting that these limiting speeds may not be the upper limit for dislocation motion [258, 264–270]. Transonic and supersonic dislocations were discovered via MD simulations in silicon and germanium by Hahn et al. [271] and Zhao et al. [272]. However, transonic (between longitudinal (c_1) and two transverse ($c_1 \geq c_3$) sound speeds) or supersonic (faster than longitudinal (c_1) and two transverse ($c_1 \geq c_3$) sound speeds) motion of dislocations has not been found in a real crystal experimentally prior to

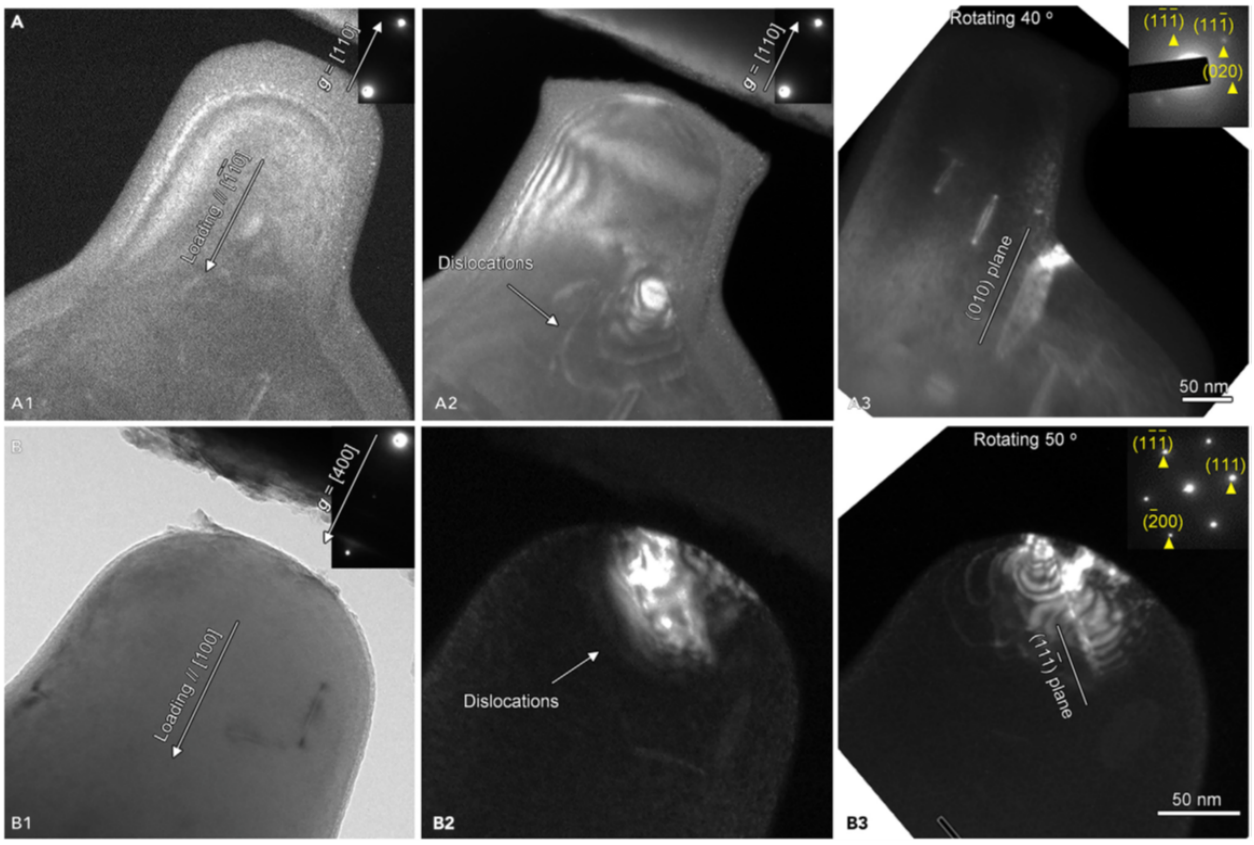

FIG. 20. Dislocations under different loading orientations in diamond. (A) Dislocations are activated along <110> orientation (A1 and A2). The slip plane is rotated to present its edge-on view (A3) and identified as (010) plane. (B) Dislocations are activated along <100> orientation (B1 and B2). The slip plane is rotated to present its edge-on view (B3) and identified as (111) plane [76].

the work by Katagiri et al. [169]. At strain rates higher than 10^7 s^{-1}, shock compression can generate dislocations whose initial speed exceeds the limiting speed due to the discontinuity of energy at the shock wavefront. Shock-induced transonic dislocation motion in single crystal diamond is demonstrated experimentally by femtosecond x-ray radiography [169]. The peak shock pressures were 184 ± 16 GPa and 92 ± 15 GPa along [100] and [110] orientations, respectively, which are high enough to induce yielding in diamond [177], resulting in strong shear stresses which trigger failure mechanisms. The shock wavefront splits into a preceding elastic front and a following plastic front where dislocations propagate

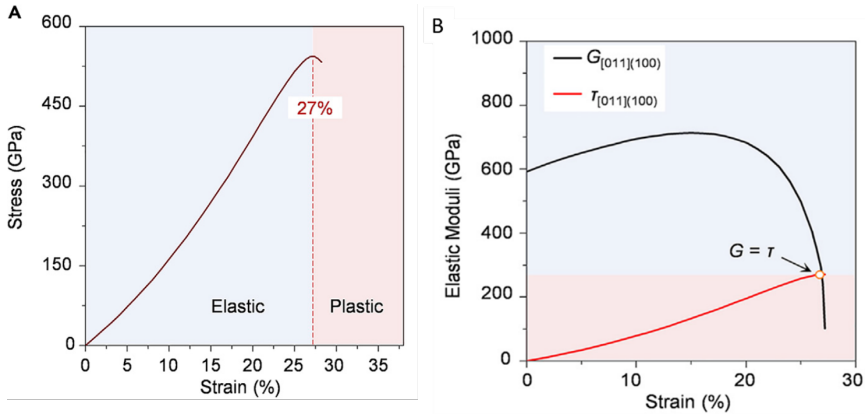

FIG. 21. (A) Theoretical stress-strain curve of compressed diamond along [111] orientation. The first stress drop/plateau occurs at 27% strain and corresponds to the onset of plasticity. (B) Shear modulus $G_{[011](100)}$ and resolved shear stress $\tau_{[011](100)}$ of the {100}<110> slip system [76].

during shock compression. These are captured by x-ray radiography along the [110] orientation, moving across the diamond sample from the lower to the upper part of Figure 16. Shock induced amorphous bands diagonal to the shock wavefront were observed in other brittle materials [272–278]; however, the estimated temperature in shocked diamond is below 20% of the melting point, which is insufficient to induce amorphization. The possibility of phase transition is also minimal since the applied stress is significantly below the threshold of phase transformation [7, 212]. Transonic dislocations can be induced at energy or displacement discontinuities present at a shock wavefront [279, 280]. A perfect dislocation splits into partial dislocations under these conditions, resulting in a stacking fault in between which expands the plastically deformed volume [281, 282]. In Figure 17, the presence of stacking faults is in the form of discontinuous lines, suggesting that the dislocations propagate along with the plastic wavefront from the side of the diamond surface shocked by laser. Figure 16 shows in [110] shock direction, the bands do not appear in the plastic wavefront center, because the majority of the dislocations propagating with the plastic wavefront are from the limited region of the diamond surface shocked by laser. This suggests that the number of newly formed dislocations at the plastic wavefront is much less than those originated from the shocked diamond surface. In Figure 18, dislocation velocity (v_d) and longitudinal

and transverse sound speeds (c_1, c_2, and c_3) of diamond are shown as a function of the density for the [110] orientation [283]. The dislocation velocities of [100] and [110] both are within the transonic regime (i.e., between c_1 and c_3). Such ultrafast dislocation motion has significant influence on the mechanical properties of materials. Since dislocation motion propagates with the plastic wavefront, increasing the shock stress to induce a faster plastic shock wave has the potential to accelerate dislocation motion even further. This opens the possibility for experimental studies of the existence of supersonic dislocations in a real crystal. Microscopic dislocation motions could potentially impact macroscopic dynamics of elastic-plastic deformation. The experimental investigation of transonic dislocation motion gives insights into the ultrafast deformation mechanisms under extreme conditions [169, 284].

TABLE 3. Third-order elastic constants of diamond (GPa) [203]

Ref.	Grimsditch, 1978	Anastassakis,1990	Cousins, 2003	Nielsen, 1986	Lang, 2011
C_{111}	-6260	-7367	-6475	-6300 ± 300	-7603 ± 600
C_{112}	-2260	-2136	-1947	-800 ± 100	-1909 ± 554
C_{123}	112	1040	982	0 ± 400	835 ± 1447
C_{144}	-674	186	115	0 ± 300	1438 ± 853
C_{166}	-2860	-3292	-2998	-2600 ± 100	-3938 ± 375
C_{456}	-823	76	-135	-1300 ± 100	-2316 ± 743

However, different interpretations of the claims of stacking fault formation and transonic dislocation motion emerged. It is argued that a brittle fracture response rather than dislocation-mediated plasticity for inelastic deformation prevails in laser shock compressed single crystal diamond [285]. Thus, brittle failure such as cracking would be an alternative deformation mechanism because direct imaging of stacking faults is too weak to be observed via the technique used by Makarov and Katagiri et al. [169, 253]. Hawreliak et al. [285] believes that the linear features in Figures 16 and 17 are not attributed to x-ray scattering caused by stacking faults or dislocations. Instead, they are due to the enhanced contrast from cracks along {111} planes via phase contrast imaging. However, this is an open question.

8.5 Ramp (Quasi-Isentropic) Compression

As mentioned in Sections 2 and 3, shock compression can generate significantly higher pressure than static compression. But the temperature rise generated by shock is so significant that above hundreds of GPa typically only fluid properties are probed into. Ramp-wave compression methods (quasi-isentropic compression) extend the pressure range for solid-state physics into the TPa regime [6, 7, 286]. Diamond was ramp-compressed to a peak pressure of 1400 GPa, and the stress-density relation along this ramp compression path was examined up to 800 GPa. Brittle materials often lose strength catastrophically when shock compression exceeds the elastic yield. However, experimental results indicate that diamond is stable and still has significant strength under ramp compression to at least 800 GPa [4].

8.6 Static Compression

Dislocation mediated plastic deformation in submicron single crystal diamond pillars via in situ mechanical testing by transmission electron microscope (TEM) was observed at room temperature by Nie et al. [76]. Dislocation generation and propagation were induced by the confinement-free compression. Figure 19 shows the evolution of a diamond nanopillar under compression test. Atomic resolution images show that mixed-type dislocations slipping are activated in the non-close-packed planes {001} with Burgers vectors 1/2<110> uniaxially compressed along <110> (Figure 20A) and <111> orientations. As for the <100> orientation compression (Figure 20B), typical dislocations are activated in the {111} planes, exhibiting strong orientation dependence. These findings give novel insights into the mechanical response of diamond and prompt reconsideration of the fundamental deformation mechanism of diamond and in other brittle covalently-bonded materials at low temperatures. The {100}<110> slip system has hardly been identified in FCC crystals at room temperature. Figure 21(A) shows the calculated stress-strain curve which drops at 27% strain of diamond under [111] uniaxial compression, Figure 21(B) exhibits its shear modulus $G_{[011](100)}$ and resolved shear stress $\tau_{[011](100)}$ for the {100}<110> slip system. The contrast between the brittle and ductile responses in diamond is explained by the competing mechanisms of Griffith cleavage [287] and plastic shear occurring at a crack tip. The strong C-C covalent bond must be broken to generate dislocations in diamond. At room temperature, breaking the C–C covalent bonds

results in cleavage fracture rather than slip. In general, the initial dislocation density in diamond is several orders of magnitude lower than that in metals, making it extremely difficult to deform plastically before cleavage sets in at room temperature [226, 288]. The stress state of a material plays a significant part in plastic deformation. High hydrostatic pressure can inhibit propagation of microcracks and trigger dislocation slip in diamond [289, 290]. The hydrostatic pressure to initiate the plastic deformation is predicted to be as high as hundreds of GPa [289], which may be achieved by indentation [71, 291] and diamond anvil cell [62, 292]. Dislocations on the {111}<110> slip systems were observed near the Knoop indentation [291], though these dislocations might pre-exist in diamond before the indentation [293]. Developments of in situ mechanical tests via electron microscopy have enabled the investigation of elastic deformation [294–296] and the direct observation of microstructural evolution in real time [297]. Both {001}<110> and {111}<110> slip systems can be triggered along different orientations. It is surprisingly easier to initiate dislocations on {001}<110> slip systems than {111}<110>, even though {111}<110> is more common in most FCC crystals. The distinctive dislocation activities in diamond are not only due to its Schmid factor but are ascribed to its intrinsic nature such as lattice parameter and C–C bonds [76]. The lack of defect generation for diamond shocked up to 69 GPa in [001] direction in pulsed laser shock compression experiments is also corroborated by TEM results of Li et al. [103]. The crystallinity of the single crystal diamond was perfectly preserved, with no plastic deformation observed and its corresponding electron diffraction pattern of the area confirmed the perfect crystalline order.

TABLE 4. Shock, ramp (quasi-isentropic), and static compression of diamond

Authors	Method	Orientation	Pressure (GPa)	Year
Shock compression				
Kondo et al. [207]	Gas gun flyer plate	Intermediate direction between <111> and <110>	191 and 217	1983
He et al. [230]	Shock wave compression by the high velocity impact of an Al foil plate driven by a pulsed laser beam.	Polycrystalline with random orientation	54, 70, 80, 142, 196	2002
Brygoo et al. [214]	Laser shock	[100]	500 to 1500	2007
Knudson et al. [212]	Shock-wave experiments using a magnetically driven flyer-plate	Polycrystalline	550 to 1400	2008
Eggert et al. [79]	Laser shock	Single-crystal and polycrystalline, with little preferred orientation.	600 to 4000	2009
McWilliams et al. [177]	Laser shock	<100>, <110>, <111>, and polycrystalline	Up to 800	2010
Lang et al. [204]	Two-stage gun	[100]	∼90 and ∼120	2010
Lang et al. [203]	Powder gun or two-stage gun	[100], [110], and [111]	Up to 120	2011
Schropp et al. [239]	Laser shock	Polycrystalline	N/A	2015
Lang et al. [205]	Single-stage powder gun and a two-stage gun	[110] and [111]	Up to ∼120	2018
MacDonald et al. [211]	Laser shock	Polycrystalline	Up to 300	2020
Winey et al. [210]	Plate impact experiments	[100], [110], and [111]	Up to ∼900	2020
Katagiri et al. [216]	Laser shock	<100>	60 to 550	2020
Jakubowska et al. [245]	Laser shock	[100]	300 to 900	2021
Katagiri et al. [243]	Laser shock	Nanopolycrystalline	Up to 707	2022
Katagiri et al. [169]	Laser shock	[100], [110], and [111]	184 ± 16 and 92 ± 15	2023
Ramp (quasi-isentropically) compression				
Bradley et al. [4]	Ramp compression	Polycrystalline	Up to 1400	2009
Smith et al. [6]	Ramp compression	Polycrystalline	Up to 5000	2014
Lazicki et al. [7]	Ramp compression	Polycrystalline	Up to 2000	2021
Static compression				
Nie et al. [76]	Nanopillar confinement-free compression	<100>, <110>, <111>	N/A	2020
Dubrovinsky [57]	Static DAC	-	Up to 600	2012

9. Diamond Experiments Performed under Ultrahigh Pressure Conditions

Diamond has played a distinguished role in extreme compression experiments. Laboratory experiments have compressed solid diamond well beyond the pressure at the center of the Earth (∼350 GPa). Diamond anvil cells have attained pressures exceeding 1000 GPa in quasi-static compression using microballs of nanocrystalline diamond [58]. Laser-driven ramp compression experiments have compressed solid diamond to ∼2000 GPa, demonstrating with in-situ X-ray diffraction it remains in the diamond-cubic phase [7]. Indeed, laser-driven ramp compression experiments to ∼5000 GPa showed no indication of melting or a transformation to another phase in the measured surface velocity or reflectivity, albeit without diffraction or any other direct probe of the crystal structure [6]. In this section we review the experiments that drove diamond to multi-TPa pressures and examine what has enabled diamond to be compressed in the solid phase to the highest pressures of any elemental solid.

Various properties of diamond make it well suited as a functional component in dynamic experiments, especially dynamic high-energy-density (HED) physics experiments and inertial confinement fusion experiments. The most important properties in this context are low atomic number (Z=6), high sound velocity, optical transparency, mechanical strength, relatively low cost (synthetic diamond), batch-to-batch consistency, (cubic) crystalline structure, high thermal conductivity, and favorable X-ray opacity. Diamond can serve as an ablator, a tamper, or a window. For example, as an ICF ablator it benefits from a sufficiently high opacity to absorb the X-rays when cold and a low opacity in the heated blow-off enabling X-rays to reach the critical surface [Lindl PoP 1995] as well as high strength to contain the DT fuel and suppress Rayleigh-Taylor instability [10]. As an HED tamper/window, its shock impedance (67 MPa-s/m) matches well to transition metals (e.g. 63, 62, and 70 MPa-s/m for Mo, Au and Pt, respectively) and its optical transparency enables it to serve as a window for Velocity interferometer System for Any Reflector (VISAR) or Particle Doppler Velocimetry (PDV) beams to probe the metal surface, unless the temperature is too high or the grain size too small in which cases it is opaque. For all these applica-

tions the ability to use chemical vapor deposition (CVD) to produce diamond with a textured columnar microstructure avoids detrimental variations in the sound speed that would otherwise result from grain-to-grain variation in the crystal orientation [Smith]. Beyond these important applications, diamond itself has been the subject of HED materials experiments, including those mentioned in the previous paragraph that drove solid diamond to extraordinary pressures, comparable to the center of the largest exoplanets, and studied its properties up to those extremes.

Diamond is resistant to melting to higher temperatures than any non-carbon elemental solid. It is also robust against shock melting to the highest shock pressures, melting at shock conditions of P $\sim$ 800 GPa and T $\sim$ 7500K [85, 214, 217, 236], with indications of melting starting at P $\sim$ 600 GPa [79]. Many of the other properties of shocked diamond are reviewed above. In contrast to shocks, ramp compression avoids generation of entropy at the shock front that is an inevitable feature of shock waves resulting from conservation of mass, momentum, and energy and the Second Law of Thermodynamics at the shock front (Rankine-Hugoniot equations). Avoiding these jump conditions, ramp waves typically result in a compression that is lower in temperature than the corresponding Hugoniot and lower in pressure [ref], although dissipative processes still generate entropy, e.g., work done against material strength. Remarkably, in some cases ramp compression of diamond can result in a higher temperature and higher pressure at a given density than the corresponding shock, as shown by Bradley et al. [4], a result of the loading-history-dependent strength of diamond.

At the time, the experiments of Bradley et al. [4] achieved the highest ramp compression pressure and the highest-pressure solid equation-of-state data obtained on any material. The diamond ramp compression experiments were conducted at the Laboratory for Laser Energetics. Using an indirect drive method, 21 beams of the OMEGA laser illuminated a metal cylinder called a hohlraum, or in this case a half-raum since the laser beams only enter one end of the cylinder. The hohlraum generated a bath of X-rays which illuminated the diamond surface. As material was ablated, the pressure on the surface increased smoothly, launching a ramp compression wave into the diamond. The wave propagated through the diamond and impinged on the free surface at the far side which was probed by a VISAR (velocity interferometer for any reflector). The diamond surface consisted of four steps each probed by the VISAR, providing four

different propagation distances for the ramp wave to transit the diamond. This geometry probed the ramp compression wave at different Lagrangian points and the resulting time differences were used to back out the Lagrangian velocity and thereby both the density and the longitudinal stress of the ramp wave in the bulk material [298]. The data were found to be considerably less stiff than the Hugoniot, consistent with a lower temperature ramp compression. Comparison of these data to predictions from first-principles models showed a somewhat stiffer equation of state than predicted by modern Thomas-Fermi-Dirac models and Density Functional Theory. The stress plateaus present in the DFT cold curve were not observed. The stiffer response could result from sample temperature, material strength and/or phase transformations.

Remarkably, a ramp-compression experiment on the NIF was able to compress solid diamond even further to 5000 GPa [6]. The density increased to 3.7 times the initial ambient diamond density, an extreme compression for the least compressible material known. The NIF is a 2-MJ laser system, much larger than the 40-kJ OMEGA laser, but in addition to the increased energy, the ultra-high-pressure ramp compression benefitted from a longer pulse duration and more accurate control of the pulse shape generating a ramp wave that did not propagate into a shock. Like the experiment of Bradley et al. [4], this was an indirect-drive ramp-compression experiment on a stepped planar target using VISAR as the only diagnostic for the material response. The resulting surface velocity measurements on four steps show a smooth compression, without abrupt changes in surface velocity or reflectivity. A Lagrangian analysis of the surface velocities yielded the stress vs. density relationship (closely related to the equation of state) [298]. These results indicate the diamond remained solid, with no indication of melting or a phase transformation to another solid crystal structure. Although the results were not definitive with regard to phase, first-principles calculations predicted a sufficiently large change in equation of state from proposed phase changes to be detectable in the experiment. The inferred stress-density relationship was consistent with the Thomas-Fermi-Dirac equation of state, as well as several density functional theory predictions.

A subsequent ramp-compression experiment on the NIF compressed solid diamond to 2000 GPa with simultaneous X-ray diffraction that showed unambiguously the carbon remained in the diamond cubic structure [7]. As discussed above, first-principles calculations predict several solid phases beyond the familiar graphite, diamond and fullerene allotropes that occur at ambient conditions. Body-centered

cubic (BC8) and simple cubic phases (SC1 and SC4) have been predicted above 1000 GPa [87, 299–301]. None of those phases was observed in the in-situ X-ray diffraction data for ramp compression up to 2000 GPa. The structure remained diamond cubic (FC8), likely as a meta-stable phase. At the time, the pressure attained in this experiment was more than twice that of any other experiment yielding solid X-ray diffraction data.

The experiment was a direct-drive ramp-compression experiment in which 16 laser beams of the NIF were used to compress the sample over 25-30 ns and hold it at high pressure and another 24 laser beams were used to illuminate a germanium or zirconium foil, creating the X-rays to probe the lattice structure through diffraction. A planar drive was attained using phase plates and by overlapping the drive beams. The foil and sample are mounted inside the TARDIS (TARget Diffraction In-Situ) X-ray diffraction diagnostic. It is an enclosure made of thick tantalum–tungsten alloy and lined with three image plates on which the diffraction data are recorded. The sample is also probed with a line VISAR to probe the surface velocity throughout the compression. The sample is a planar target, without steps. The stress is determined from the surface velocity of the tamped diamond using an equation of state measured in earlier experiments. The drive laser profile was designed to produce a leading shock of about 100 GPa, roughly corresponding to the elastic limit of diamond. The drive laser was subsequently ramped monotonically up in intensity until reaching a plateau to hold the pressure for the diffraction measurement. The samples for the initial shots measuring diamond diffraction consisted of diamond crystallites in an epoxy matrix to avoid melting the diamond from the heat generated by work against the large mechanical strength of diamond. Later shots observed that thin single-crystal diamond foils did not melt under shock-ramp compression, and they were used for the shots attaining pressure of $\sim$ 2000 GPa. The lack of melting was taken to be evidence that either the available strength models [180, 302] significantly over-predict high-pressure diamond strength, perhaps due to loss of strength in the leading shock, or a mechanism like anomalously large energy storage in defects is active, as would be evidenced by a low Taylor-Quinney factor.

10. Conclusions

Diamond is the hardest natural material because of its covalent and strong sp^3 bonding, with a characteristic Young's modulus of over 1,000 GPa and a compressive strength of at least 60 GPa. These properties make it into the choice material for cutting, drilling, and polishing of other less hard materials. Additionally, it has optical properties (transparency, coefficient of reflection) that render it attractive for a number of applications, from jewelry to optical windows. Its density, strength, chemical inertness, and specific heat also make it one of the best materials for ablation and use as the capsules containing deuterium and tritium fuel in inertial confinement fusion research. There are essentially two approaches to the study of diamond: experimental and computational. They are reviewed separately below.

10.1 Experimental Methods

1. The high pressures required for plastic deformation in diamond need specialized experiments to establish its response. These can be classified into static and shock experiments. Table 4 is a summary of the shock, ramp, and static compression experiments.

2. Quasistatic diamond strength has been studied extensively using the diamond anvil cell, where the anvils themselves can undergo deformation and fracture processes.

3. Two other techniques that provide insight into the plastic deformation of diamond are micro and nanoindentation using a shallow indenter (Knoop preferred) and nanopillar experiments followed by characterization by transmission electron microscopy.

4. In the dynamic deformation domain, gas-gun and laser shock techniques have been applied. The determination of the Hugoniot elastic limit (HEL) yields important information about the compression strength of diamond, and real-time diagnostics such as VISAR and PVD gauges enhance the understanding. Optical techniques have also been used to establish the stresses beyond which transparency is lost.

5. Diamond is a highly anisotropic material. The HEL was measured by several investigators [177, 207, 220]. McWilliams et al. [177] found HEL to be orientation dependent: 80 GPa for [100], 81 GPa for [110], and 60 GPa for [111]. This orientation dependence is consistent with the difficulty of emitting

dislocations in nanopillar experiments. For the [100] orientation, the resolved shear stress is much lower for (100) slip.

6. Diamond loses its transparency for quasistatic loading at about 40 GPa. In shock compression, the transparency is lost only at 170 GPa. However, it is lost upon unloading from lower stress levels. This is attributed to defects in the lattice.

7. Although transonic and even supersonic dislocations have been predicted in molecular dynamics calculations, there is only one report on transonic partial dislocation motion in laser-shocked diamond by Katagiri et al. [169]. This observation was disputed by another group and therefore this is still an open area of inquiry.

8. Experiments at the National Ignition Facility (LLNL) at ultrahigh pressures (up to 2000 GPa) in ramp compression coupled with VISAR diagnostics revealed that diamond still retains its strength and diamond cubic structure.

9. Melting occurs for shock compression of diamond, at a temperature of $\sim$8000 K and pressure of $\sim$800 GPa. This is the prediction from the Rankine-Hugoniot conservation equations. However, if the pressure is ramped with a much slower rise, in a quasi-isentropic mode, much higher pressures can be achieved in the solid state. This stratagem has been successfully used in NIF and Omega to reach pressures of 1000 to 5000 GPa.

10. Some exoplanets contain a great amount of carbon in their interior. The extreme conditions of these solid-state core materials intrigue the interest in exploring the nature of carbon under ultrahigh pressure. It is vital to understand the evolution and structure of high-pressure and high-temperature behavior and phases and to develop equation of state models.

11. Natural diamond has formed in the upper mantle of the Earth from metallic melts at temperatures of 900–1,400 °C and pressures of 5–6 GPa over 1 to 3 billion years. Synthetic diamond was first developed in 1950s. Currently, there are two mature methods to grow synthetic diamonds. One is chemical vapor deposition (CVD), and the other is high pressure and high temperature (HPHT) growth. Recently, Gong et al. [303] were able to synthesize diamond under a moderate temperature of 1,025 °C and at an unprecedented 1 atm pressure compared to the 1300-1600 °C and 5-6 GPa (50,000-60,000 atmospheres)

of HPHT method.

12. Ramp compression experiments to multi-Terapascal pressures have shown the extraordinary stability of the diamond phase under compression. X-ray diffraction confirms the retention of the cubic phase up to 2 TPa. Even in experiments up to 5 TPa, measures of surface velocity and reflectivity show no evidence of a phase change.

10.2 Computational Methods

1. Although several computational methods have been used, by far the most predominant is molecular dynamics. A variety of potentials have been used for the simulation of diamond, with different focuses from recreating its physical properties with the most accuracy, to simulating its chemical reactions more reliably. A summary of the strengths and developments of these classical potentials is given in Table 1.

2. One of the first potentials to be used was the Tersoff. It is a rather simple potential, but several of its derivatives still find widespread use today, and can be used to predict shock effects such as dislocation generation and motion.

3. Beyond the simpler potentials, quantum mechanical calculations utilizing the Schrodinger equation with the Born-Oppenheimer approximation can be implemented for different materials using the density functional theory (DFT). These types of calculations are extremely computationally intensive, limited to dozens or hundreds of atoms at a time, but are currently the most accurate we can produce. They are especially useful in investigating temperature and pressure regions where performing experiments is difficult and classical potentials may be inaccurate. Investigation into the high pressure phase transformations of diamond has required the use of DFT and AIMD, and identified areas where improved experiments and measurement techniques may expand our understanding of diamond.

4. Machine Learning Potentials provide quantum-level accuracy at a computational load that make billion atom simulations possible over nanosecond timescales, approaching real experimentally observable conditions. They function by fitting some form of descriptive method to large datasets of quantum mechanical data, and interpolating between the data without having to perform the costly quantum mechanical calculations at each point.

5. Machine Learning Potentials still have drawbacks. They are still not as fast as the classical potentials that are based on a physical formulation, and can be unreliable when attempting to describe events that were not included in their training dataset, such as defects and dislocations, chemical reactions, or diffusion.

Acknowledgments

This work was supported by the LDRD program at Lawrence Livermore National Laboratory (21-ERD-032) and Center for Matter under Extreme Conditions (CMEC) under Department of Energy-National Nuclear Security Administration Grant No. DE-NA0004147. This work was performed in part under the auspices of the U.S. Department of Energy by LLNL under Contract DE-AC52-07NA27344. EMB thank support from grant PICTO-UUMM-2019-00048 from the Argentinean Agencia-I+D+i.

References

[1]A. Demming, *King of the elements?*, Nanotechnology **21**, 300201 (2010).

[2]Y. Xu, *et al.*, *A diamond-bearing core-mantle boundary on Mercury*, Nature Communications **15**, 5061 (2024).

[3]K. Nguyen-Cong, *et al.*, *Extreme metastability of diamond and its transformation to the BC8 post-diamond phase of carbon*, The Journal of Physical Chemistry Letters **15**, 1152–1160 (2024).

[4]D. Bradley, *et al.*, *Diamond at 800 GPa*, Physical Review Letters **102**, 075503 (2009).

[5]D. C. Swift, *et al.*, *Shock formation and the ideal shape of ramp compression waves*, Physical Review E **78**, 066115 (2008).

[6]R. F. Smith, *et al.*, *Ramp compression of diamond to five terapascals*, Nature **511**, 330–333 (2014).

[7]A. Lazicki, *et al.*, *Metastability of diamond ramp-compressed to 2 terapascals*, Nature **589**, 532–535 (2021).

[8]D. Roundy and M. L. Cohen, *Ideal strength of diamond, Si, and Ge*, Physical Review B **64**, 212103 (2001).

[9]J. Field, *The mechanical and strength properties of diamond*, Reports on Progress in Physics **75**, 126505 (2012).

[10]J. Biener, *et al.*, *Diamond spheres for inertial confinement fusion*, Nuclear Fusion **49**, 112001 (2009).

[11]T. Stachel and J. W. Harris, *Formation of diamond in the earth's mantle*, Journal of Physics: Condensed Matter **21**, 364206

(2009).

[12]J. K. Russell, L. A. Porritt, Y. Lavallée, and D. B. Dingwell, *Kimberlite ascent by assimilation-fuelled buoyancy*, Nature **481**, 352–356 (2012).

[13]F. Bundy, H. T. Hall, H. Strong, and R. Wentorfjun, *Man-made diamonds*, Nature **176**, 51–55 (1955).

[14]F. P. Bundy, H. P. Bovenkerk, H. M. Strong, and R. H. Wentorf Jr, *Diamond-graphite equilibrium line from growth and graphitization of diamond*, The Journal of Chemical Physics **35**, 383–391 (1961).

[15]F. Bundy, *Direct conversion of graphite to diamond in static pressure apparatus*, The Journal of Chemical Physics **38**, 631–643 (1963).

[16]P. S. DeCarli and J. C. Jamieson, *Formation of diamond by explosive shock*, Science **133**, 1821–1822 (1961).

[17]B. Derjaguin, *et al.*, *Filamentary diamond crystals*, Journal of Crystal Growth **2**, 380–384 (1968).

[18]B. Spitsyn, L. Bouilov, and B. Derjaguin, *Vapor growth of diamond on diamond and other surfaces*, Journal of Crystal Growth **52**, 219–226 (1981).

[19]S. Matsumoto, Y. Sato, M. Kamo, and N. Setaka, *Vapor deposition of diamond particles from methane*, Japanese Journal of Applied Physics **21**, L183 (1982).

[20]Y. Hirose, S. Amanuma, and K. Komaki, *The synthesis of high-quality diamond in combustion flames*, Journal of Applied Physics **68**, 6401–6405 (1990).

[21]K. Kurihara, K. Sasaki, M. Kawarada, and N. Koshino, *High rate synthesis of diamond by dc plasma jet chemical vapor deposition*, Applied Physics Letters **52**, 437–438 (1988).

[22]N. Ohtake and M. Yoshikawa, *Diamond film preparation by arc discharge plasma jet chemical vapor deposition in the methane atmosphere*, Journal of the Electrochemical Society **137**, 717 (1990).

[23]S. Ferro, *Synthesis of diamond*, Journal of Materials Chemistry **12**, 2843–2855 (2002).

[24]C.-s. Yan, Y. K. Vohra, H.-k. Mao, and R. J. Hemley, *Very high growth rate chemical vapor deposition of single-crystal diamond*, Proceedings of the National Academy of Sciences **99**, 12523–12525 (2002).

[25]Q. Liang, *et al.*, *Recent advances in high-growth rate single-crystal CVD diamond*, Diamond and Related Materials **18**, 698–703 (2009).

[26]M. Schreck, S. Gsell, R. Brescia, and M. Fischer, *Ion bombardment induced buried lateral growth: The key mechanism for*

the synthesis of single crystal diamond wafers, Scientific reports **7**, 44462 (2017).

[27]W. Gust, *Phase transition and shock-compression parameters to 120 GPa for three types of graphite and for amorphous carbon*, Physical Review B **22**, 4744 (1980).

[28]L. F. Trueb, *An electron-microscope study of shock-synthesized diamond*, Journal of Applied Physics **39**, 4707–4716 (1968).

[29]P. S. Decarli, *Shock wave synthesis of diamond and other phases*, MRS Online Proceedings Library (OPL) **383**, 21 (1995).

[30]D. Erskine and W. Nellis, *Shock-induced martensitic phase transformation of oriented graphite to diamond*, Nature **349**, 317–319 (1991).

[31]D. Kraus, *et al.*, *Nanosecond formation of diamond and lonsdaleite by shock compression of graphite*, Nature Communications **7**, 10970 (2016).

[32]V. Sobolev, Y. Taran, and S. Gubenko, *Shock wave use for diamond synthesis*, Le Journal de Physique IV **7**, C3–73 (1997).

[33]H. Hirai and K.-i. Kondo, *Modified phases of diamond formed under shock compression and rapid quenching*, Science **253**, 772–774 (1991).

[34]E. Wheeler and D. Lewis, *The structure of a shock-quenched diamond*, Materials Research Bulletin **10**, 687–693 (1975).

[35]F. P. Bundy, *The p, t phase and reaction diagram for elemental carbon, 1979*, Journal of Geophysical Research: Solid Earth **85**, 6930–6936 (1980).

[36]M. E. Lipschutz and E. Anders, *The record in the meteorites—IV: Origin of diamonds in iron meteorites*, Geochimica et Cosmochimica Acta **24**, 83–105 (1961).

[37]E. Anders, *Diamonds in meteorites*, Scientific American **213**, 26–37 (1965).

[38]R. Hanneman, H. Strong, and F. Bundy, *Hexagonal diamonds in meteorites: Implications*, Science **155**, 995–997 (1967).

[39]P. Németh, *et al.*, *Shock-formed carbon materials with intergrown sp3-and sp2-bonded nanostructured units*, Proceedings of the National Academy of Sciences **119**, e2203672119 (2022).

[40]R. Hough, *et al.*, *Diamond and silicon carbide in impact melt rock from the Ries impact crater*, Nature **378**, 41–44 (1995).

[41]C. Koeberl, *et al.*, *Diamonds from the Popigai impact structure, Russia*, Geology **25**, 967–970 (1997).

[42]R. S. Clarke Jr, D. E. Appleman, and D. R. Ross, *An antarctic iron meteorite contains preterrestrial impact-produced diamond and lonsdaleite*, Nature **291**, 396–398 (1981).

[43]J. Smith and J. Dawson, *Carbonado: Diamond aggregates from early impacts of crystal rocks?*, Geology **13**, 342–343 (1985).

[44]N. R. Greiner, D. Phillips, J. Johnson, and F. Volk, *Diamonds in detonation soot*, Nature **333**, 440–442 (1988).

[45]K. V. Volkov, V. V. Danilenko, and V. Elin, *Synthesis of diamond from the carbon in the detonation products of explosives*, Combustion, Explosion and Shock Waves **26**, 366–368 (1990).

[46]N. N. Thadhani, *Shock-induced chemical reactions and synthesis of materials*, Progress in Materials Science **37**, 117–226 (1993).

[47]S.-S. Shang, K. Hokamoto, and M. Meyers, *Hot dynamic consolidation of hard ceramics*, Journal of materials science **27**, 5470–5476 (1992).

[48]D. K. Potter and T. J. Ahrens, *Shock consolidation of diamond and graphite mixtures to fused polycrystalline diamond*, Journal of applied physics **63**, 910–914 (1988).

[49]K. Hokamoto, M. Fujita, S. Tanaka, T. Kodama, and Y. Ujimoto, *High-temperature shock consolidation of diamond powders using converging underwater shock wave*, Scripta Materialia **39**, 1383–1388 (1998).

[50]T. Akashi and A. B. Sawaoka, *Shock consolidation of diamond powders*, Journal of materials science **22**, 3276–3286 (1987).

[51]K.-I. Kondo, S. Kukino, and H. Hirai, *Shock-compaction of nano-sized diamond powder, as examined by microstructural analysis*, Journal of the American Ceramic Society **79**, 97–101 (1996).

[52]J. Field and C. Pickles, *Strength, fracture and friction properties of diamond*, Diamond and Related Materials **5**, 625–634 (1996).

[53]B. Willems, P. Martineau, D. Fisher, J. Van Royen, and G. Van Tendeloo, *Dislocation distributions in brown diamond*, Physica Status Solidi (a) **203**, 3076–3080 (2006).

[54]U. Bangert, R. Barnes, M. Gass, A. Bleloch, and I. Godfrey, *Vacancy clusters, dislocations and brown colouration in diamond*, Journal of Physics: Condensed Matter **21**, 364208 (2009).

[55]D. Fisher, *Brown diamonds and high pressure high temperature treatment*, Lithos **112**, 619–624 (2009).

[56]J. C. Jamieson, A. Lawson, and N. Nachtrieb, *New device for obtaining x-ray diffraction patterns from substances exposed to high pressure*, Review of Scientific instruments **30**, 1016–1019 (1959).

[57]L. Dubrovinsky, N. Dubrovinskaia, V. B. Prakapenka, and A. M. Abakumov, *Implementation of micro-ball nanodiamond anvils for high-pressure studies above 6 Mbar*, Nature Communications **3** (2012).

[58]N. Dubrovinskaia, *et al.*, *Terapascal static pressure generation with ultrahigh yield strength nanodiamond*, Science advances **2**, e1600341 (2016).

[59]W. A. Bassett, *Diamond anvil cell, 50th birthday*, High Pressure Research **29**, 163–186 (2009).

[60]A. Jayaraman, *Diamond anvil cell and high-pressure physical investigations*, Reviews of Modern Physics **55**, 65 (1983).

[61]S. Anzellini and S. Boccato, *A practical review of the laser-heated diamond anvil cell for university laboratories and synchrotron applications*, Crystals **10**, 459 (2020).

[62]H. Mao, P. Bell, K. Dunn, R. Chrenko, and R. DeVries, *Absolute pressure measurements and analysis of diamonds subjected to maximum static pressures of 1.3–1.7 Mbar*, Review of Scientific Instruments **50**, 1002–1009 (1979).

[63]B. Li, *et al.*, *Diamond anvil cell behavior up to 4 Mbar*, Proceedings of the National Academy of Sciences **115**, 1713–1717 (2018).

[64]J.-J. Zhao, S. Scandolo, J. Kohanoff, G. Chiarotti, and E. Tosatti, *Elasticity and mechanical instabilities of diamond at megabar stresses: Implications for diamond-anvil-cell research*, Applied Physics Letters **75**, 487–488 (1999).

[65]J. Liu and Y. K. Vohra, *Fluorescence emission from high purity synthetic diamond anvil to 370 GPa*, Applied Physics Letters **68**, 2049–2051 (1996).

[66]J.-a. Xu and H.-k. Mao, *Moissanite: A window for high-pressure experiments*, Science **290**, 783–785 (2000).

[67]J.-a. Xu, H.-k. Mao, and R. J. Hemley, *The gem anvil cell: High-pressure behaviour of diamond and related materials*, Journal of Physics: Condensed Matter **14**, 11549 (2002).

[68]H. Wu, X. Luo, L. Wen, H. Sun, and C. Chen, *Extreme static compression of carbon to terapascal pressures*, Carbon **144**, 161–170 (2019).

[69]F. Knoop, C. G. Peters, and W. B. Emerson, *A sensitive pyramidal-diamond tool for indentation measurements*, Journal of Research of the National Bureau of standards **23**, 39 (1939).

[70]H. Sumiya and Y. Ishida, *Real hardness of high-purity ultra-fine nano-polycrystalline diamond synthesized by direct conversion sintering under HPHT*, Diamond and Related Materials **100**, 107560 (2019).

[71]P. Humble and R. Hannink, *Plastic deformation of diamond at room temperature*, Nature **273**, 37–39 (1978).

[72]M. M. Chaudhri, *Indentation hardness of diamond single crystals, nanopolycrystal, and nanotwinned diamonds: A critical review*, Diamond and Related Materials **109**, 108076 (2020).

[73]A. Richter, R. Ries, R. Smith, M. Henkel, and B. Wolf, *Nanoindentation of diamond, graphite and fullerene films*, Diamond and Related Materials **9**, 170–184 (2000).

[74]J. Xiong, *et al.*, *Mechanical properties evaluation of diamond films via nanoindentation*, Diamond and Related Materials **130**, 109403 (2022), URL https://www.sciencedirect.com/science/article/pii/S0925963522005854.

[75]T. Sawa and K. Tanaka, *Nanoindentation of natural diamond*, Philosophical Magazine A **82**, 1851–1856 (2002), URL https://doi.org/10.1080/01418610208235696, https://doi.org/10.1080/01418610208235696.

[76]A. Nie, *et al.*, *Direct observation of room-temperature dislocation plasticity in diamond*, Matter **2**, 1222–1232 (2020).

[77]Y. Bu, P. Wang, A. Nie, and H. Wang, *Room-temperature plasticity in diamond*, Science China Technological Sciences **64**, 32–36 (2021).

[78]B. Regan, *et al.*, *Plastic deformation of single-crystal diamond nanopillars*, Advanced Materials **32**, 1906458 (2020).

[79]J. Eggert, *et al.*, *Melting temperature of diamond at ultrahigh pressure*, Nature Physics **6**, 40–43 (2010).

[80]X. Wang, S. Scandolo, and R. Car, *Carbon phase diagram from ab initio molecular dynamics*, Physical review letters **95**, 185701 (2005).

[81]A. A. Correa, S. A. Bonev, and G. Galli, *Carbon under extreme conditions: Phase boundaries and electronic properties from first-principles theory*, Proceedings of the National Academy of Sciences **103**, 1204–1208 (2006).

[82]L. X. Benedict, *et al.*, *Multiphase equation of state for carbon addressing high pressures and temperatures*, Physical Review B **89**, 224109 (2014).

[83]D. Young and R. Grover, *Theory of the carbon phase diagram at high pressures and temperatures*, Tech. Rep., Lawrence Livermore National Lab., CA (USA) (1987).

[84]J. Shi, *et al.*, *Double-Shock Compression Pathways from Diamond to BC8 Carbon*, Physical Review Letters **131**, 146101 (2023), URL https://link.aps.org/doi/10.1103/PhysRevLett.131.146101, Publisher: American Physical Society.

[85]J. T. Willman, *et al.*, *Machine learning interatomic potential for simulations of carbon at extreme conditions*, Physical Review B **106**, L180101 (2022).

[86]A. Correa, S. A. Bonev, and G. Galli, *Carbon under extreme conditions: phase boundaries and electronic properties from first-principles theory.*, Proceedings of the National Academy of Sciences **103**, 1204–8 (2006), URL http://www.pubmedcentral.nih.gov/articlerender.fcgi?artid=1345714&tool=pmcentrez&rendertype=abstract.

[87]S. Scandolo, G. L. Chiarotti, and E. Tosatti, *SC4: A metallic phase of carbon at terapascal pressures*, Physical Review B **53**, 5051–5054 (1996), URL https://link.aps.org/doi/10.1103/PhysRevB.53.5051, Publisher: American Physical Society.

[88]J. Sun, D. D. Klug, and R. Martoňák, *Structural transformations in carbon under extreme pressure: Beyond diamond*, The Journal of Chemical Physics **130**, 194512 (2009), URL https://doi.org/10.1063/1.3139060.

[89]C. Frondel and U. B. Marvin, *Lonsdaleite, a hexagonal polymorph of diamond*, Nature **214**, 587–589 (1967).

[90]F. Bundy and J. Kasper, *Hexagonal diamond—a new form of carbon*, The Journal of Chemical Physics **46**, 3437–3446 (1967).

[91]P. Nemeth, *et al.*, *Lonsdaleite is faulted and twinned cubic diamond and does not exist as a discrete material*, Nature Communications **5** (2014).

[92]Q. Li, Y. Sun, Z. Li, and Y. Zhou, *Lonsdaleite - a material stronger and stiffer than diamond*, Scripta Materialia **65**, 229–232 (2011).

[93]Z. Pan, H. Sun, Y. Zhang, and C. Chen, *Harder than diamond: Superior indentation strength of wurtzite BN and lonsdaleite*, Physical Review Letters **102** (2009).

[94]E. Güler and M. Güler, *Elastic and mechanical properties of hexagonal diamond under pressure*, Applied Physics A **119**, 721–726 (2015).

[95]V. V. Brazhkin and V. L. Solozhenko, *Myths about new ultrahard phases: Why materials that are significantly superior to diamond in elastic moduli and hardness are impossible*, Journal of Applied Physics **125** (2019).

[96]A. Kelly and N. H. MacMillan, *Strong Solids* (Clarendon Press, 1986).

[97]T. J. Volz and Y. M. Gupta, *Elastic moduli of hexagonal diamond and cubic diamond formed under shock compression*, Physical Review B **103** (2021).

[98]J. Tersoff, *New empirical approach for the structure and energy of covalent systems*, Physical review B **37**, 6991 (1988).

[99]J. Nord, K. Albe, P. Erhart, and K. Nordlund, *Modelling of compound semiconductors: Analytical bond-order potential for*

gallium, nitrogen and gallium nitride, Journal of Physics: Condensed Matter **15**, 5649 (2003).

[100]Z. Sha, P. Branicio, Q. Pei, V. Sorkin, and Y. Zhang, *A modified Tersoff potential for pure and hydrogenated diamond-like carbon*, Computational Materials Science **67**, 146–150 (2013).

[101]L. Shi, *et al.*, *Molecular dynamics simulation of phonon thermal transport in nanotwinned diamond with a new optimized Tersoff potential*, Physical Chemistry Chemical Physics **23**, 8336–8343 (2021).

[102]P. Wang, *et al.*, *Dislocation-mediated brittle-ductile transition of diamond under high pressure*, Diamond and Related Materials **138**, 110198 (2023).

[103]A. C. Li, B. Li, R. E. Rudd, and M. A. Meyers, *Dislocation generation in diamond under extreme loading*, Matter **6**, 3040–3056 (2023).

[104]G. He, C. Xu, C. Liu, H. Liu, and H. Wang, *Grain size and temperature effects on the indentation induced plastic deformations of nano polycrystalline diamond*, Applied Surface Science **480**, 349–360 (2019).

[105]Q. Zhang, *et al.*, *Designing ultrahard nanostructured diamond through internal defects and interface engineering at different length scales*, Carbon **170**, 394–402 (2020).

[106]G. G. Vidable, *et al.*, *Simulations of plasticity in diamond nanoparticles showing ultrahigh strength*, Diamond and Related Materials **126**, 109109 (2022).

[107]F. Aquistapace, *et al.*, *Plasticity in diamond nanoparticles: Dislocations and amorphization during loading and dislocation multiplication during unloading*, Journal of Materials Science **59**, 4788–4809 (2024).

[108]P. Erhart and K. Albe, *Analytical potential for atomistic simulations of silicon, carbon, and silicon carbide*, Physical Review B **71**, 035211 (2005).

[109]B. Wen, *et al.*, *Continuous strengthening in nanotwinned diamond*, npj Computational Materials **5**, 117 (2019).

[110]F. H. Stillinger and T. A. Weber, *Computer simulation of local order in condensed phases of silicon*, Physical Review B **31**, 5262–5271 (1985).

[111]P. Mahon, B. Pailthorpe, and G. Bacskay, *A quantum mechanical calculation of interatomic interactions in diamond*, Philosophical Magazine B **63**, 1419–1430 (1991).

[112]A. Barnard and S. Russo, *Development of an improved Stillinger-Weber potential for tetrahedral carbon using ab initio (Hartree-Fock and MP2) methods*, Molecular Physics **100**, 1517–1525 (2002).

[113]A. Barnard, S. Russo, and G. Leach, *Nearest neighbour considerations in Stillinger-Weber type potentials for diamond*, Molecular Simulation **28**, 761–771 (2002).

[114]D. W. Brenner, *Empirical potential for hydrocarbons for use in simulating the chemical vapor deposition of diamond films*, Physical Review B **42**, 9458 (1990).

[115]S. V. Zybin, M. L. Elert, and C. T. White, *Orientation dependence of shock-induced chemistry in diamond*, Physical Review B - Condensed Matter and Materials Physics **66**, 1–4 (2002).

[116]J. N. Glosli and F. H. Ree, *The melting line of diamond determined via atomistic computer simulations*, The Journal of Chemical Physics **110**, 441–446 (1999).

[117]R. Perriot, X. Gu, Y. Lin, V. V. Zhakhovsky, and I. I. Oleynik, *Screened environment-dependent reactive empirical bond-order potential for atomistic simulations of carbon materials*, Physical Review B—Condensed Matter and Materials Physics **88**, 064101 (2013).

[118]S. J. Stuart, A. B. Tutein, and J. A. Harrison, *A reactive potential for hydrocarbons with intermolecular interactions*, The Journal of Chemical Physics **112**, 6472–6486 (2000).

[119]T. C. O'Connor, J. Andzelm, and M. O. Robbins, *AIREBO-M: A reactive model for hydrocarbons at extreme pressures*, The Journal of Chemical Physics **142** (2015).

[120]B.-J. Lee and J. W. Lee, *A modified embedded atom method interatomic potential for carbon*, Calphad **29**, 7–16 (2005).

[121]L. S. Liyanage, *et al.*, *Structural, elastic, and thermal properties of cementite (Fe3C) calculated using a modified embedded atom method*, Physical Review B **89**, 094102 (2014).

[122]C. Xu, C. Wang, C. T. Chan, and K. Ho, *A transferable tight-binding potential for carbon*, Journal of Physics: Condensed Matter **4**, 6047 (1992).

[123]L. Goodwin, *A new tight binding parameterization for carbon*, Journal of Physics: Condensed Matter **3**, 3869 (1991).

[124]D. Porezag, T. Frauenheim, T. Köhler, G. Seifert, and R. Kaschner, *Construction of tight-binding-like potentials on the basis of density-functional theory: Application to carbon*, Physical Review B **51**, 12947 (1995).

[125]A. Thess, *et al.*, *Crystalline ropes of metallic carbon nanotubes*, Science **273**, 483–487 (1996).

[126]D. Qian, G. J. Wagner, W. K. Liu, M.-F. Yu, and R. S. Ruoff, *Mechanics of carbon nanotubes*, Appl. Mech. Rev. **55**, 495–533 (2002).

[127]J. Morris, C. Fu, and K. Ho, *Tight-binding study of tilt grain boundaries in diamond*, Physical Review B **54**, 132 (1996).

[128]N. Marks, *Modelling diamond-like carbon with the environment-dependent interaction potential*, Journal of Physics: Condensed Matter **14**, 2901 (2002).

[129]J. Buchan, *et al.*, *Molecular dynamics simulation of radiation damage cascades in diamond*, Journal of Applied Physics **117** (2015).

[130]F. J. Valencia, *et al.*, *Nanoindentation of amorphous carbon: A combined experimental and simulation approach*, Acta Materialia **203**, 116485 (2021).

[131]A. C. Van Duin, S. Dasgupta, F. Lorant, and W. A. Goddard, *ReaxFF: A reactive force field for hydrocarbons*, The Journal of Physical Chemistry A **105**, 9396–9409 (2001).

[132]K. Chenoweth, A. C. Van Duin, and W. A. Goddard, *ReaxFF reactive force field for molecular dynamics simulations of hydrocarbon oxidation*, The Journal of Physical Chemistry A **112**, 1040–1053 (2008).

[133]S. G. Srinivasan, A. C. Van Duin, and P. Ganesh, *Development of a ReaxFF potential for carbon condensed phases and its application to the thermal fragmentation of a large fullerene*, The Journal of Physical Chemistry A **119**, 571–580 (2015).

[134]J. Los and A. Fasolino, *Intrinsic long-range bond-order potential for carbon: Performance in Monte Carlo simulations of graphitization*, Physical Review B **68**, 024107 (2003).

[135]J. H. Los, L. M. Ghiringhelli, E. J. Meijer, and A. Fasolino, *Improved long-range reactive bond-order potential for carbon. I. construction*, Physical Review B—Condensed Matter and Materials Physics **72**, 214102 (2005).

[136]L. M. Ghiringhelli, J. H. Los, E. J. Meijer, A. Fasolino, and D. Frenkel, *Modeling the phase diagram of carbon*, Physical Review Letters **94**, 145701 (2005).

[137]T. Wen, L. Zhang, H. Wang, E. Weinan, and D. J. Srolovitz, *Deep potentials for materials science*, Materials Futures **1**, 022601 (2022).

[138]Y. Mishin, *Machine-learning interatomic potentials for materials science*, Acta Materialia **214**, 116980 (2021).

[139]V. Eyert, J. Wormald, W. A. Curtin, and E. Wimmer, *Machine-learned interatomic potentials: Recent developments and prospective applications*, Journal of Materials Research **38**, 5079–5094 (2023).

[140]G. Wang, *et al.*, *Machine learning interatomic potential: Bridge the gap between small-scale models and realistic device-scale simulations*, iScience **27** (2024).

[141]E. V. Podryabinkin, E. V. Tikhonov, A. V. Shapeev, and A. R. Oganov, *Accelerating crystal structure prediction by machine-learning interatomic potentials with active learning*, Physical Review B **99**, 064114 (2019).

[142]A. P. Bartók, M. C. Payne, R. Kondor, and G. Csányi, *Gaussian approximation potentials: The accuracy of quantum mechanics, without the electrons*, Physical review letters **104**, 136403 (2010).

[143]V. L. Deringer, *et al.*, *Gaussian process regression for materials and molecules*, Chemical Reviews **121**, 10073–10141 (2021).

[144]P. Rowe, V. L. Deringer, P. Gasparotto, G. Csányi, and A. Michaelides, *An accurate and transferable machine learning potential for carbon*, The Journal of Chemical Physics **153** (2020).

[145]Y. Wang, Z. Fan, P. Qian, T. Ala-Nissila, and M. A. Caro, *Structure and pore size distribution in nanoporous carbon*, Chemistry of Materials **34**, 617–628 (2022).

[146]A. P. Thompson, L. P. Swiler, C. R. Trott, S. M. Foiles, and G. J. Tucker, *Spectral neighbor analysis method for automated generation of quantum-accurate interatomic potentials*, Journal of Computational Physics **285**, 316–330 (2015).

[147]K. Nguyen-Cong, *et al.*, *Billion atom molecular dynamics simulations of carbon at extreme conditions and experimental time and length scales*, In *Proceedings of the International Conference for High Performance Computing, Networking, Storage and Analysis*, 1–12 (2021).

[148]J. T. Willman, *et al.*, *Accuracy, transferability, and computational efficiency of interatomic potentials for simulations of carbon under extreme conditions*, The Journal of Chemical Physics **161** (2024).

[149]R. Z. Khaliullin, H. Eshet, T. D. Kühne, J. Behler, and M. Parrinello, *Graphite-diamond phase coexistence study employing a neural-network mapping of the ab initio potential energy surface*, Physical Review B—Condensed Matter and Materials Physics **81**, 100103 (2010).

[150]P. Yoo, *et al.*, *Neural network reactive force field for C, H, N, and O systems*, npj Computational Materials **7**, 9 (2021).

[151]Y. Shaidu, *et al.*, *A systematic approach to generating accurate neural network potentials: The case of carbon*, npj Computational Materials **7**, 52 (2021).

[152]J. Wang, *et al.*, *A deep learning interatomic potential developed for atomistic simulation of carbon materials*, Carbon **186**, 1–8 (2022).

[153]Z. Fan, *et al.*, *GPUMD: A package for constructing accurate machine-learned potentials and performing highly efficient*

atomistic simulations, The Journal of Chemical Physics **157**, 114801 (2022).

[154]H. Dong, *et al.*, *Molecular dynamics simulations of heat transport using machine-learned potentials: A mini-review and tutorial on GPUMD with neuroevolution potentials*, Journal of Applied Physics **135** (2024).

[155]M. Wen and E. B. Tadmor, *Uncertainty quantification in molecular simulations with dropout neural network potentials*, npj computational materials **6**, 124 (2020).

[156]M. Qamar, M. Mrovec, Y. Lysogorskiy, A. Bochkarev, and R. Drautz, *Atomic cluster expansion for quantum-accurate large-scale simulations of carbon*, Journal of Chemical Theory and Computation **19**, 5151–5167 (2023).

[157]R. K. Lindsey, L. E. Fried, and N. Goldman, *Chimes: A force matched potential with explicit three-body interactions for molten carbon*, Journal of chemical theory and computation **13**, 6222–6229 (2017).

[158]R. Lindsey, *et al.*, *ChIMES carbon 2.0: A transferable machine-learned interatomic model harnessing multifidelity training data*, ChemRxiv (2024).

[159]I. S. Novikov, K. Gubaev, E. V. Podryabinkin, and A. V. Shapeev, *The MLIP package: Moment tensor potentials with MPI and active learning*, Machine Learning: Science and Technology **2**, 025002 (2020).

[160]S. R. Xie, M. Rupp, and R. G. Hennig, *Ultra-fast interpretable machine-learning potentials*, npj Computational Materials **9**, 162 (2023).

[161]M. MacIsaac, S. Bavdekar, D. Spearot, and G. Subhash, *A genetic algorithm trained machine-learned interatomic potential for the silicon–carbon system*, The Journal of Physical Chemistry C **128**, 12213–12226 (2024).

[162]J. Vandermause, *et al.*, *On-the-fly active learning of interpretable bayesian force fields for atomistic rare events*, npj Computational Materials **6**, 20 (2020).

[163]J. Zeng, *et al.*, *DeePMD-kit v2: A software package for deep potential models*, The Journal of Chemical Physics **159** (2023).

[164]K. Chen, *et al.*, *Exploring phase change and structure of carbon using deep learning interatomic potential*, Physical Chemistry Chemical Physics (2024).

[165]T. Chen, Q. Liu, Y. Liu, L. Sun, and M. Chen, *Combining stochastic density functional theory with deep potential molecular dynamics to study warm dense matter*, Matter and Radiation at Extremes **9** (2024).

[166]G.-W. Chen, *et al.*, *The transformation mechanism of graphite to hexagonal diamond under shock conditions*, JACS Au

(2024).

[167]G. A. Marchant, M. A. Caro, B. Karasulu, and L. B. Pártay, *Exploring the configuration space of elemental carbon with empirical and machine learned interatomic potentials*, npj Computational Materials **9**, 131 (2023).

[168]Y. Liu and Y. Mo, *Learning from models: High-dimensional analyses on the performance of machine learning interatomic potentials*, npj Computational Materials **10**, 159 (2024).

[169]K. Katagiri, *et al.*, *Transonic dislocation propagation in diamond*, Science **382**, 69–72 (2023), URL https://www.science.org.

[170]A. P. Thompson, *et al.*, *LAMMPS - a flexible simulation tool for particle-based materials modeling at the atomic, meso, and continuum scales*, Computer Physics Communications **271**, 108171 (2022).

[171]D. Lu, *et al.*, *DP compress: A model compression scheme for generating efficient deep potential models*, Journal of chemical theory and computation **18**, 5559–5567 (2022).

[172]J. Tersoff, *Modeling solid-state chemistry: Interatomic potentials for multicomponent systems*, Physical Review B **39**, 5566–5568 (1989).

[173]A. Musaelian, *et al.*, *Learning local equivariant representations for large-scale atomistic dynamics*, Nature Communications **14**, 579 (2023).

[174]R. Z. Khaliullin, H. Eshet, T. D. Kühne, J. Behler, and M. Parrinello, *Graphite-diamond phase coexistence study employing a neural-network mapping of the ab initio potential energy surface*, Physical Review B **81**, 100103 (2010).

[175]D. R. Robinson and M. Wilson, *The liquid ↔ amorphous transition and the high pressure phase diagram of carbon*, Journal of Physics: Condensed Matter **25**, 155101 (2013).

[176]N. D. Mermin, *Thermal properties of the inhomogeneous electron gas*, Physical Review **137**, A1441 (1965).

[177]R. S. McWilliams, *et al.*, *Strength effects in diamond under shock compression from 0.1 to 1 TPa*, Phys. Rev. B **81**, 014111 (2010), URL https://link.aps.org/doi/10.1103/PhysRevB.81.014111.

[178]M. Millot, *et al.*, *High-precision shock equation of state measurements for metallic fluid carbon between 15 and 20 Mbar*, Physics of Plasmas **27**, 102711 (2020), URL https://doi.org/10.1063/5.0007304http://aip.scitation.org/doi/10.1063/5.0007304.

[179]S. Zhang, K. P. Driver, F. Soubiran, and B. Militzer, *First-principles equation of state and shock compression predictions of*

warm dense hydrocarbons, Phys. Rev. E **96**, 013204 (2017), URL https://link.aps.org/doi/10.1103/PhysRevE.96.013204.

[180]D. C. Swift, *et al.*, *Equation of state and strength of diamond in high-pressure ramp loading*, Physical Review B **105**, 014109 (2022).

[181]F. González-Cataldo, B. K. Godwal, K. P. Driver, R. Jeanloz, and B. Militzer, *Model of ramp compression of diamond from ab initio simulations*, Physical Review B **104**, 134104 (2021), URL https://link.aps.org/doi/10.1103/PhysRevB.104.134104.

[182]K. Nguyen-Cong, A. S. Williams, J. T. Willman, A. B. Belonoshko, and I. I. Oleynik, *First principles molecular dynamics simulations of high-pressure melting of diamond*, In *AIP Conference Proceedings*, vol. 2272, 070010 (2020), URL http://aip.scitation.org/doi/abs/10.1063/12.0001100.

[183]R. F. Smith, *et al.*, *Equation of state of iron under core conditions of large rocky exoplanets*, Nature Astronomy **2**, 452–458 (2018), URL http://www.nature.com/articles/s41550-018-0437-9.

[184]C. C. Battaile, D. J. Srolovitz, and J. Butler, *A kinetic Monte Carlo method for the atomic-scale simulation of chemical vapor deposition: Application to diamond*, Journal of Applied Physics **82**, 6293–6300 (1997).

[185]P. W. May, N. L. Allan, M. N. Ashfold, J. C. Richley, and Y. A. Mankelevich, *Simplified Monte Carlo simulations of chemical vapour deposition diamond growth*, Journal of Physics: Condensed Matter **21**, 364203 (2009).

[186]M. Frenklach, *Monte carlo simulation of diamond growth by methyl and acetylene reactions*, The Journal of chemical physics **97**, 5794–5802 (1992).

[187]W. Rodgers, P. May, N. Allan, and J. Harvey, *Three-dimensional kinetic monte carlo simulations of diamond chemical vapor deposition*, The Journal of Chemical Physics **142** (2015).

[188]M. Eckert, E. Neyts, and A. Bogaerts, *Insights into the growth of (ultra) nanocrystalline diamond by combined molecular dynamics and Monte Carlo simulations*, Crystal Growth & Design **10**, 3005–3021 (2010).

[189]K. P. Driver and B. Militzer, *All-electron path integral monte carlo simulations of warm dense matter:<? format?> application to water and carbon plasmas*, Physical Review Letters **108**, 115502 (2012).

[190]D. Saumon, G. Chabrier, and H. M. van Horn, *An equation of state for low-mass stars and giant planets*, Astrophysical Journal Supplement v. 99, p. 713 **99**, 713 (1995).

[191]T. Guillot, *Interiors of giant planets inside and outside the solar system*, Science **286**, 72–77 (1999), URL https://www.science.org.

[192]W. Hubbard, *et al.*, *Interior structure of neptune: Comparison with Uranus*, Science **253**, 648–651 (1991).

[193]M. Ross, *The ice layer in Uranus and Neptune—diamonds in the sky?*, Nature **292**, 435–436 (1981).

[194]F. Ancilotto, G. L. Chiarotti, S. Scandolo, and E. Tosatti, *Dissociation of methane into hydrocarbons at extreme (planetary) pressure and temperature*, Science **275**, 1288–1290 (1997).

[195]L. R. Benedetti, *et al.*, *Dissociation of CH4 at high pressures and temperatures: Diamond formation in giant planet interiors?*, Science **286**, 100–102 (1999), URL https://www.science.org.

[196]D. Kraus, *et al.*, *Formation of diamonds in laser-compressed hydrocarbons at planetary interior conditions*, Nature Astronomy **1**, 606–611 (2017).

[197]B. Cheng, S. Hamel, and M. Bethkenhagen, *Thermodynamics of diamond formation from hydrocarbon mixtures in planets*, Nature Communications **14**, 1104 (2023).

[198]J. C. Bond, D. P. O'Brien, and D. S. Lauretta, *The compositional diversity of extrasolar terrestrial planets. I. in situ simulations*, Astrop. J. **715**, 1050 (2010).

[199]H. F. Wilson and B. Militzer, *Interior phase transformations and mass–radius relationships of silicon–carbon planets*, The Astrophysical Journal **793**, 34 (2014).

[200]N. Madhusudhan, K. K. Lee, and O. Mousis, *A possible carbon-rich interior in super-Earth 55 Cancri e*, The Astrophysical Journal Letters **759**, L40 (2012).

[201]P. E. Nissen, *The carbon-to-oxygen ratio in stars with planets*, Astronomy & Astrophysics **552**, A73 (2013).

[202]R. Hu, *et al.*, *A secondary atmosphere on the rocky exoplanet 55 Cancri e*, Nature 1–2 (2024).

[203]J. M. Lang and Y. M. Gupta, *Experimental determination of third-order elastic constants of diamond*, Physical Review Letters **106** (2011).

[204]J. M. Lang and Y. M. Gupta, *Strength and elastic deformation of natural and synthetic diamond crystals shock compressed along [100]*, Journal of Applied Physics **107** (2010).

[205]J. M. Lang, J. M. Winey, and Y. M. Gupta, *Strength and deformation of shocked diamond single crystals: Orientation dependence*, Physical Review B **97** (2018).

[206]R. Grover, *Does diamond melt?*, The Journal of Chemical Physics **71**, 3824–3829 (1979).

[207]K.-i. Kondo and T. J. Ahrens, *Shock compression of diamond crystal*, Geophysical Research Letters **10**, 281–284 (1983).

[208]M. Pavlovsky, *Shock compressibility of six very hard substances*, Sov Phys Solid State **12**, 1736–1737 (1971).

[209]R. McQueen and S. Marsh, *Hugoniots of graphites of various initial densities and the equation of state of carbon.*, Tech. Rep., Los Alamos Scientific Lab., N. Mex. (1967).

[210]J. M. Winey, M. D. Knudson, and Y. M. Gupta, *Shock compression response of diamond single crystals at multimegabar stresses*, Physical Review B **101** (2020).

[211]M. J. MacDonald, *et al.*, *Using simultaneous x-ray diffraction and velocity interferometry to determine material strength in shock-compressed diamond*, Applied Physics Letters **116** (2020).

[212]M. Knudson, M. Desjarlais, and D. Dolan, *Shock-wave exploration of the high-pressure phases of carbon*, Science **322**, 1822–1825 (2008).

[213]D. G. Hicks, *et al.*, *High-precision measurements of the diamond hugoniot in and above the melt region*, Physical Review B - Condensed Matter and Materials Physics **78** (2008).

[214]S. Brygoo, *et al.*, *Laser-shock compression of diamond and evidence of a negative-slope melting curve*, Nature Materials **6**, 274–277 (2007).

[215]M. C. Gregor, *et al.*, *Hugoniot and release measurements in diamond shocked up to 26 mbar*, Physical Review B **95** (2017).

[216]K. Katagiri, *et al.*, *Shock response of full density nanopolycrystalline diamond*, Physical Review Letters **125** (2020).

[217]H. Nagao, *et al.*, *Hugoniot measurement of diamond under laser shock compression up to 2 TPa*, Physics of Plasmas **13** (2006).

[218]M. A. Meyers, *Dynamic Behavior of Materials* (John Wiley & Sons, 1994), URL https://onlinelibrary.wiley.com/doi/book/10.1002/9780470172278.

[219]E. E. McBride, *et al.*, *Phase transition lowering in dynamically compressed silicon*, Nature Physics **15**, 89–94 (2019).

[220]J. M. Lang Jr, *Mechanical and optical response of diamond crystals shock compressed along different orientations* (Washington State University, 2013).

[221]Y. M. Gupta, *Stress dependence of elastic-wave attenuation in lif*, Journal of Applied Physics **46**, 3395–3401 (1975).

[222]J. P. Hirth and J. Lothe, *Theory of Dislocations* (McGraw-Hill, 1968).

[223]J. J. Gilman, *Micromechanics of Flow in Solids* (McGraw-Hill, 1969).

[224]C. Dang, *et al.*, *Achieving large uniform tensile elasticity in microfabricated diamond*, Science **371**, 76–78 (2021).

[225]R. Telling, C. Pickard, M. Payne, and J. Field, *Theoretical strength and cleavage of diamond*, Physical review letters **84**, 5160 (2000).

[226]J. E. Field, *The mechanical and strength properties of diamond*, Reports on Progress in Physics **75** (2012).

[227]D. E. Grady, *Shock deformation of brittle solids.*, Journal of Geophysical Research **85**, 913–924 (1980).

[228]H. K. Mao and P. M. Bell, *High-pressure physics: Sustained static generation of 1.36 to 1.72 megabars*, Science **200**, 1145–1147 (1978).

[229]Y. G. Gogotsi, A. A. Kailer, and N. K. G., *Transformation of diamond to graphite*, Nature **401**, 663–664 (1999).

[230]H. He, T. Sekine, and T. Kobayashi, *Direct transformation of cubic diamond to hexagonal diamond*, Applied Physics Letters **81**, 610–612 (2002).

[231]F. Bundy, *et al.*, *The pressure-temperature phase and transformation diagram for carbon; updated through 1994*, Carbon **34**, 141–153 (1996).

[232]M. P. Grumbach and R. M. Martin, *Phase diagram of carbon at high pressures and temperatures*, Physical review B **54**, 15730 (1996).

[233]L. E. Fried and W. M. Howard, *Explicit Gibbs free energy equation of state applied to the carbon phase diagram*, Physical Review B **61**, 8734 (2000).

[234]J. Morris, C. Wang, and K. Ho, *Relationship between structure and conductivity in liquid carbon*, Physical Review B **52**, 4138 (1995).

[235]M. K. Matzen, *Z pinches as intense x-ray sources for high-energy density physics applications*, Physics of Plasmas **4**, 1519–1527 (1997), URL https://doi.org/10.1063/1.872323, https://pubs.aip.org/aip/pop/article-pdf/4/5/1519/19308804/1519_1_online.pdf.

[236]M. N. Pavlovskii, *Shock compression of diamond*, Soviet Physics Solid State, Ussr **13**, 741 (1971).

[237]J. E. Field, *The Properties of natural and synthetic diamond* (Academic Press, 1992).

[238]M. I. Eremets, *et al.*, *The strength of diamond*, Applied Physics Letters **87**, 1–3 (2005).

[239]A. Schropp, *et al.*, *Imaging shock waves in diamond with both high temporal and spatial resolution at an XFEL*, Scientific

Reports **5** (2015).

[240]M. I. Eremets, *et al.*, *Refractive index of diamond under pressure*, High Pressure Research **9**, 347–350 (1992).

[241]K. Katagiri, *et al.*, *Optical properties of shock-compressed diamond up to 550 GPa*, Physical Review B **101**, 184106 (2020).

[242]L. Margulies, G. Winther, and H. F. Poulsen, *In situ measurement of grain rotation during deformation of polycrystals*, Science **291**, 2392–2394 (2001).

[243]K. Katagiri, *et al.*, *Strength of diamond beyond the elastic limit under dynamic compression*, arXiv preprint arXiv:2208.03416 (2022).

[244]K. Momma and F. Izumi, *VESTA 3 for three-dimensional visualization of crystal, volumetric and morphology data*, Journal of applied crystallography **44**, 1272–1276 (2011).

[245]K. Jakubowska, *et al.*, *Reflecting laser-driven shocks in diamond in the megabar pressure range*, High power laser science and engineering **9**, e3 (2021).

[246]Q. Johnson, A. Mitchell, and E. L., *X-ray diffraction evidence for crystalline order and isotropic compression during the shock-wave process*, Nature **231**, 310–311 (1971).

[247]M. A. Meyers and K. K. Chawla, *Mechanical behavior of materials* (Cambridge university press, 2008).

[248]R. Madec, B. Devincre, L. Kubin, T. Hoc, and D. Rodney, *The role of collinear interaction in dislocation-induced hardening*, Science **301**, 1879–1882 (2003).

[249]T. Irifune, K. A., S. S., T. Inoue, and H. Sumiya, *Ultrahard polycrystalline diamond from graphite*, Nature **421**, 599–600 (2003).

[250]T. Ishikawa, *et al.*, *A compact X-ray free-electron laser emitting in the sub-ångström region*, Nature Photonics **6**, 540–544 (2012).

[251]R. A. Graham and W. P. Brooks, *Shock-wave compression of sapphire from 15 to 420 kbar. the effects of large anisotropic compressions*, J. Phys. Chem. Solids **32**, 2311–2330 (1971).

[252]S. Bavdekar and G. Subhash, *Comparison of pressure-sensitive strength models for ceramics under ultrahigh confinement*, International Journal of Impact Engineering **118**, 60–66 (2018).

[253]S. Makarov, *et al.*, *Direct imaging of shock wave splitting in diamond at Mbar pressure*, Matter and Radiation at Extremes

8 (2023).

[254]W. G. Johnston and J. J. Gilman, *Dislocation multiplication in lithium fluoride crystals*, Journal of Applied Physics **31**, 632–643 (1960).

[255]M. Meyers, *et al.*, *Chapter 89 dislocations in shock compression and release*, Dislocations in Solids **15**, 91–197 (2009).

[256]H. Fan, Q. Wang, J. A. El-Awady, D. Raabe, and M. Zaiser, *Strain rate dependency of dislocation plasticity*, Nature Communications **12**, 1845 (2021).

[257]L. A. Zepeda-Ruiz, A. Stukowski, T. Oppelstrup, and V. V. Bulatov, *Probing the limits of metal plasticity with molecular dynamics simulations*, Nature **550**, 492–495 (2017).

[258]P. Gumbsch and H. Gao, *Dislocations faster than the speed of sound*, Science **283**, 965–968 (1999).

[259]L. J. Teutonico, *Dynamical behavior of dislocations in anisotropic media*, Physical Review **124**, 1039 (1961).

[260]L. J. Teutonico, *Uniformly moving dislocations of arbitrary orientation in anisotropic media*, Physical Review **127**, 413 (1962).

[261]D. N. Blaschke, J. Chen, S. Fensin, and B. A. Szajewski, *Clarifying the definition of 'transonic' screw dislocations*, Philosophical Magazine **101**, 997–1018 (2021).

[262]J. Weertman and J. R. Weertman, *in Moving Dislocations*, vol. 3, 1–59 (North Holland Pub. Co., 1980).

[263]J. D. Eshelby, *Uniformly moving dislocations*, Proceedings of the Physical Society **Section A 62**, 307–314 (1949).

[264]H. Tsuzuki, P. S. Branicio, and J. P. Rino, *Accelerating dislocations to transonic and supersonic speeds in anisotropic metals*, Applied Physics Letters **92** (2008).

[265]Z. Jin, H. Gao, and P. Gumbsch, *Energy radiation and limiting speeds of fast moving edge dislocations in tungsten*, Physical Review B - Condensed Matter and Materials Physics **77**, 094303 (2008).

[266]S. Peng, Y. Wei, Z. Jin, and W. Yang, *Supersonic screw dislocations gliding at the shear wave speed*, Physical Review Letters **122**, 045501 (2019).

[267]P. Gumbsch and H. Gao, *Driving force and nucleation of supersonic dislocations*, Journal of Computer-Aided Materials Design **6**, 137–144 (1999).

[268]J. Weertman, *Uniformly moving transonic and supersonic dislocations*, Journal of Applied Physics **38**, 5293–5301 (1967).

[269]T. Duong and M. J. Demkowicz, *Resonance with surface waves induces forbidden velocity bands in dislocation glide*,

Journal of the Mechanics and Physics of Solids **180**, 105422 (2023).

[270]B. Gurrutxaga-Lerma, J. Verschueren, A. P. Sutton, and D. Dini, *The mechanics and physics of high-speed dislocations: A critical review*, International Materials Reviews **66**, 215–255 (2021).

[271]E. Hahn, S. Zhao, E. M. Bringa, and M. A. Meyers, *Supersonic dislocation bursts in silicon*, Scientific reports **6**, 26977 (2016).

[272]S. Zhao, *et al.*, *Generating gradient germanium nanostructures by shock-induced amorphization and crystallization*, Proceedings of the National Academy of Sciences of the United States of America **114**, 9791–9796 (2017).

[273]S. Zhao, *et al.*, *Amorphization and nanocrystallization of silicon under shock compression*, Acta Materialia **103**, 519–533 (2016).

[274]S. Zhao, *et al.*, *Directional amorphization of boron carbide subjected to laser shock compression*, Proceedings of the National Academy of Sciences **113**, 12088–12093 (2016).

[275]Zhao, Shiteng, *et al.*, *Shock-induced amorphization in covalently bonded solids*, EPJ Web Conf. **183**, 03027 (2018), URL https://doi.org/10.1051/epjconf/201818303027.

[276]S. Zhao, *et al.*, *Shock-induced amorphization in silicon carbide*, Acta Materialia **158**, 206–213 (2018).

[277]S. Zhao, *et al.*, *Directional amorphization of covalently-bonded solids: A generalized deformation mechanism in extreme loading*, Materials Today **49**, 59–67 (2021).

[278]M. Chen, J. W. Mccauley, and K. J. Hemker, *Shock-induced localized amorphization in boron carbide*, Science **299**, 1563–1566 (2003), URL https://www.science.org.

[279]A. N. Stroh, *Steady state problems in anisotropic elasticity*, Journal of Mathematics and Physics **41**, 77–103 (1962).

[280]P. M. Anderson, J. P. Hirth, and J. Lothe, *Theory of Dislocations* (Cambridge University Press, 2017).

[281]S. Masuya, K. Hanada, T. Oshima, H. Sumiya, and M. Kasu, *Formation of stacking fault and dislocation behavior during the high-temperature annealing of single-crystal HPHT diamond*, Diamond and Related Materials **75**, 155–160 (2017).

[282]J. A. Vandersall and B. D. Wirth, *Supersonic dislocation stability and nano-twin formation at high strain rate*, Philosophical Magazine **84**, 3755–3769 (2004).

[283]M. Núñez Valdez, K. Umemoto, and R. M. Wentzcovitch, *Elasticity of diamond at high pressures and temperatures*, Applied Physics Letters **101** (2012).

[284]M. D. Knudson and C. T. Seagle, *Damaging diamond with shock waves*, Science **382**, 37–38 (2023).

[285]J. A. Hawreliak, J. Winey, S. Sharma, Y. M. Gupta, *et al.*, *Comments regarding transonic dislocation propagation in diamond by katagiri, et al.(science 382, 69-72, 2023)*, arXiv preprint arXiv:2401.04213 (2024).

[286]D. K. Bradley, *et al.*, *Shock compressing diamond to a conducting fluid*, Physical Review Letters **93**, 195506 (2004).

[287]A. A. Griffith, *The phenomena of rupture and flow in solids*, 163–198 (Philosophical transactions of the royal society of London., 1921).

[288]J. E. Field and C. J. Freeman, *Strength and fracture properties of diamond*, Philosophical Magazine A: Physics of Condensed Matter, Structure, Defects and Mechanical Properties **43**, 595–618 (1981).

[289]S. Ogata and J. Li, *Toughness scale from first principles*, Journal of Applied Physics **106** (2009).

[290]P. W. Bridgman, *The effect of hydrostatic pressure on the fracture of brittle substances*, Journal of Applied Physics **18**, 246–258 (1947).

[291]H. Sumiya, K. Yamaguchi, and S. Ogata, *Deformation microstructure of high-quality synthetic diamond crystal subjected to Knoop indentation*, Applied Physics Letters **88** (2006).

[292]D. J. Weidner, Y. Wang, and M. T. Vaughan, *Strength of diamond*, Science **266**, 419–422 (1994).

[293]J. Wilks and E. Wilks, *Properties and applications of diamond* (Butterworth- Heinemann Oxford, 1991).

[294]A. Banerjee, *et al.*, *Ultralarge elastic deformation of nanoscale diamond*, Science **360**, 300–302 (2018).

[295]A. Nie, *et al.*, *Approaching diamond's theoretical elasticity and strength limits*, Nature Communications **10**, 5533 (2019).

[296]J. M. Wheeler, *et al.*, *Approaching the limits of strength: Measuring the uniaxial compressive strength of diamond at small scales*, Nano Letters **16**, 812–816 (2016).

[297]B. Y. Liu, *et al.*, *Large plasticity in magnesium mediated by pyramidal dislocations*, Science **365**, 73–75 (2019).

[298]S. Rothman, *et al.*, *Measurement of the principal isentropes of lead and lead–antimony alloy to 400 kbar by quasi-isentropic compression*, Journal of Physics D: Applied Physics **38**, 733 (2005).

[299]M. Yin and M. L. Cohen, *Will diamond transform under megabar pressures?*, Physical review letters **50**, 2006 (1983).

[300]R. Biswas, R. M. Martin, R. Needs, and O. Nielsen, *Stability and electronic properties of complex structures of silicon and carbon under pressure: Density-functional calculations*, Physical Review B **35**, 9559 (1987).

[301]M. Martinez-Canales, C. J. Pickard, and R. J. Needs, *Thermodynamically stable phases of carbon at multiterapascal*

pressures, Physical review letters **108**, 045704 (2012).

[302]D. Orlikowski, *et al.*, *A Steinberg-Guinan Model for High-Pressure Carbon: Diamond Phase*, In *AIP Conference Proceedings*, vol. 955, 247–250 (2007), URL http://aip.scitation.org/doi/abs/10.1063/1.2833022.

[303]Y. Gong, *et al.*, *Growth of diamond in liquid metal at 1 atm pressure*, Nature **629**, 348–354 (2024).